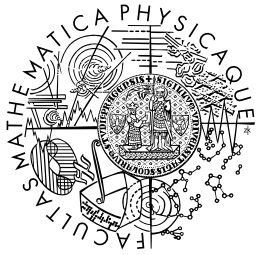

FACULTY
OF MATHEMATICS
AND PHYSICS
Charles University

MASTER THESIS

Bc. Marek Raja

Transport properties of perovskites

Institute of Physics Charles University

Supervisor of the master thesis: doc. Ing. Eduard Belas, CSc.
Study programme: Physics
Study branch: Optics and Optoelectronics

Prague 2022

I declare that I carried out this master thesis independently, and only with the cited sources, literature and other professional sources. It has not been used to obtain another or the same degree.

I understand that my work relates to the rights and obligations under the Act No. 121/2000 Sb., the Copyright Act, as amended, in particular the fact that the Charles University has the right to conclude a license agreement on the use of this work as a school work pursuant to Section 60 subsection 1 of the Copyright Act.

In ..... date ....

Author's signature

I would especially like to thank the supervisor of my master's thesis doc. Ing. Eduard Belas, CSc. for dedicated help in creating this work, from theoretical introduction to the issue, through experimental data acquisition, interpretation of the obtained results, and especially to the valuable advice of processing the work itself. Further, I would like to thank prof. RNDr. Roman Grill, DrSc. for a deeper explanation of necessary optoelectronic theories and to assist in the interpretation of the results obtained. An integral part of the team was also RNDr. Jindřich Pipek and Mgr. Marián Betušiak. Many thanks for their help and patience in explaining the functionality of specialized data analysis software.

And lastly, I would like to thank my family for their support and help in everything I do.

Title: Transport properties of perovskites

Author: Bc. Marek Raja

An Institute: Institute of Physics Charles University

Supervisor: doc. Ing. Eduard Belas, CSc., Institute of Physics Charles University

Abstract: This work studies charge transport in halide perovskites made of methylammonium lead tribromide $MAPbBr_3$. By finding and using bipolar pulsation parameters, we describe the transport properties of both holes and electrons. The shapes of the measured current waveforms with the L-TCT method are simulated by the Monte Carlo simulations. Theoretical models of charge density distribution are based on a drift-diffusion equation with consideration of the infinite and finite lifetime of a charge carrier caused by a shallow and deep trap. The obtained values of drift mobility, electric field profile, transit time, and surface recombination rate are obtained by Monte Carlo simulation. We have successfully shown the effect of pulsing with unipolar and bipolar biases. By finding the pulsation parameters at which the sample does not polarize, we calculated the hole mobility around $13\,\mathrm{cm^2V^{-1}s^{-1}}$. We arrived at the ambiguity of determining the effect of the expanding deep trap region and the effect of space charge formation. Thus, we found multiple possible models to describe the measured current waveforms. This work confirms the high sensitivity of perovskites to the method and history of measurement.

Keywords: perovskites, transient currents, charge transport, bipolar bias pulses, charge generation

Contents

1. Introduction

1.1 Motivation

For the last two decades, halide perovskites have been identified as one of the most promising materials in photovoltaic and light emitting devices such as low-cost solid-state lighting with tunable colours and narrow emission line widths at high photoluminescence quantum yields [9], [10], [22], [23]. This led to breakthroughs in materials science. In photovoltaic theoretical efficiency limit is 29% [24]. Even though it's almost the same efficient as silicon [25], the production cost of perovskites is the engine that drives current research forward. So perovskites combine both high light efficiency and low costs simultaneously. The efficiency of the organometallic halide perovskite solar cells increased significantly from 3.8% in 2009 to over 25% in 2020 [26]. Among the wide compositional range of halide perovskites, methylammonium lead tribromide perovskite $CH_3NH_3PbBr_3$ ($MAPbBr_3$) received the most attention for its potential applications in tandem solar cells, radiation detectors, and light-emitting diodes [27] and [28].

Despite all the promising results so far, perovskites hide many unexplained problems which play a critical role in the performance. The most significant influences include oxygen degradation in the air without the use of any type of encapsulation, moisture-induced degradation, and temperature-induced degradation [29]. All these mechanisms disrupt the internal structure of the material, reducing overall efficiency and functionality. However, the parameters of defects and their interplay with free-charge carriers remain unclear and that's why we are dealing with these perovskites.

In this work, we explore the dynamics of free holes and electrons in methylammonium lead tribromide single crystals using time-of-flight laser induced transient current spectroscopy (ToF L-TCT). Combining with Monte Carlo simulation we created models of the behaviour of a moving charge including mobility, the electric field inside the detector, and possible traps. The movement of weakly bound methylammonium ions was suppressed by bipolar bias pulsation coupled with the pulsation of light. The main aim of this work is to show the meaning of bipolar pulsation instead of unipolar pulsation and to develop a theoretical description of the measured current dependencies and so behaviour of free charge.

1.2 Laser-induced Transient Current Technique

There are so many methods to investigate the physical properties of radiation detectors. For our purpose to evaluate detector behaviour such as carrier mobility, electric field profile inside the detector, etc. we chose *Time-of-Flight* (ToF) type measurement called *Laser-induced Transient Current Technique* (L-TCT). Let's introduce the method in detail.

The TCT current spectroscopy is in general based on analyzing a transient current generated by charge carriers drifting through the sample under an applied bias. Charge carriers can be created by many possibilities as high speed particles, light or radioactive radiation. For our measurements, we chose laser light as the source and therefore the naming L-TCT (*Laser-induced* TCT). Principle diagram

is shown in figure 1.1. Due to the above-band-gap energy of light, light close to the surface forms electron-hole pairs. Transient current is induced by drifting electron-hole pairs created by light pulse. All drifting mechanism is possible due to the electric field inside the detector created by applied bias on contacts. Depending on the polarity of the applied bias, either the electron or the hole is picked up by the contact and the other type of charge starts to drift through the detector. Thanks to the Shockley-Ramo theorem, drifting carriers induce electric current, which is measured by an oscilloscope. The shape of collected current curves depends on factors such as applied bias, size of the detector, intensity of light pulses and so on.

But also other drifting charge carriers, such as ions, can affect measured current dependencies! Transient current is detectable until the drifting electrons and holes are collected by the contacts or are trapped inside the detector.

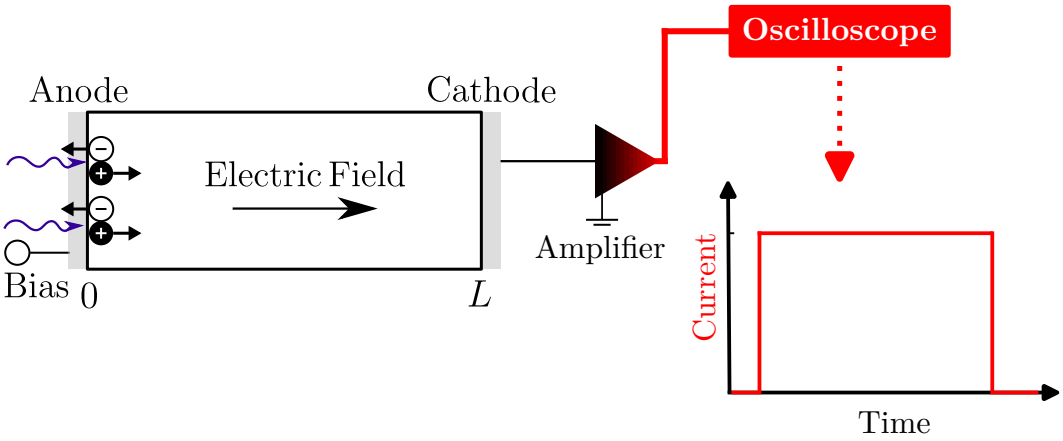

Figure 1.1: Principle diagram of L-TCT.

1.3 Perovskites

The first perovskite structure material was the calcium titanium oxide mineral $CaTiO_3$, discovered by Gustav Rose in 1839, and named after the Russian nobleman and mineralogist Count Lev Alekseyevich von Perovski [1]. Few years later, in 1926, Victor Goldschmidt firstly used perovskites as a general term for the crystal structure group [2].

Perovskites involve a huge family of materials, usually described by general chemical formula ABX_3 [13]. 3D structured perovskite can be described by cubic contractual formula of $A^{+1}B^{+2}\left(X^{-1}\right)_3$ shown in figure 1.2, where each A (an organic group or an inorganic cation) has twelve neighboring X (halide atoms), and each B (a metal cation) connects with six adjacent X through ionic bounds [14]. When a suitable organic molecule is choosen as the A cation (e.g. methylammonium MA^+: $CH_3NH_3^+$ or formamidinium FA^+: $CH\left(NH_2\right)_2^+$), the resulting material is an inorganic-organic hybrid metal halide perovskite (MHP). On the other hand, if the A cation is an inorganic atom, such as cesium (Cs^+), the resulting compound is and inorganic MHP [14].

This work explores transport properties of only methylammonium lead tribromide perovskites.

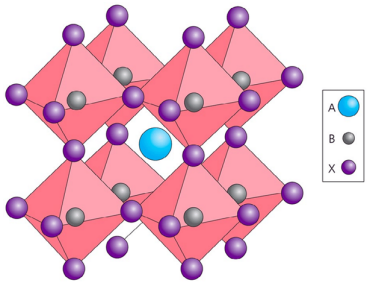

Figure 1.2: Schematic representation of simple 3D structured perovskite cell. Cubic contractual formula of $A^{+1}B^{+2}(X^{-1})_3$. Retrieved from https://www.solarchoice.net.au/blog/news/perovskites-the-next-solar-pv-revolution-240714/.

2. Kinematics of Charge Carriers in Detector

We will consider a one-dimensional approximation, so all spatial coordinates will be derived in one axis only. But first, let's start with general expressions.

2.1 Drift Mobility

Particles in the material generally move randomly. If they are surrounded by other particles, collisions occur. It is assumed that after each scattering event the carrier's motion is randomized, so it has zero average velocity. Applying voltage, after the collision, the particle accelerates in the electric field until the next collision. The resulting average drift mobility can be expressed

$$\mu = \frac{q}{m^*} \langle \tau \rangle , \tag{2.1}$$

where q is the elementary charge, m^* is the carrier effective mass and $\langle \tau \rangle$ is the average scattering time. A particle's effective mass is the mass that it seems to have when responding to forces. At room temperature, the mobility is limited mainly by collisions with crystal lattice vibrations (scattering on phonons).

2.2 Continuity Equation

2.2.1 General Form

When describing charge transport in semiconductors in the classical approximation we will use the continuity equation. The general continuity equation for holes can be written as

$$\frac{\partial p}{\partial t} = -\frac{1}{q} \nabla \cdot \mathbf{j}_h + (G_h - R_h) , \tag{2.2}$$

where p is concentration of holes, $\mathbf{j}_h$ is the hole current density, e is the elementary charge and G_h, R_h represents the hole generation and recombination. The hole current density $\mathbf{j}_h$ can be derived from the drift-diffusion equation with constant temperature

$$\mathbf{j}_h = qp\mu_h \mathbf{E} - qD_h \nabla p, \tag{2.3}$$

where μ_h is the hole mobility, $\mathbf{E}$ is the electric field intensity and D_h is the hole diffusion coefficient described by the Einstein relation

$$D_h = \mu_h \frac{k_B T}{e}, \tag{2.4}$$

where k_T is the Boltzmann constant and T is the absolute temperature.

For electrons situation is analogical. So we obtain the electron continuity equation

$$\frac{\partial n}{\partial t} = \frac{1}{q} \nabla \cdot \mathbf{j}_e + (G_e - R_e) \tag{2.5}$$

with the electron drift-diffusion equation

$$\mathbf{j}_e = qn\mu_e\mathbf{E} + qD_e\nabla n, \tag{2.6}$$

where the subscript e indicates electrons and n means concentration of electrons. The first part of drift-diffusion equations 2.3 and 2.6 indicates the drift motion of particles and the second part describes diffusion current. For the total current density $\mathbf{j}$ formed by electrons $\mathbf{j}_e$ and holes $\mathbf{j}_h$, we can write

$$\mathbf{j} = \mathbf{j}_e + \mathbf{j}_h. \tag{2.7}$$

We assume constant temperature during the whole measurement process.

2.2.2 1D Form

Let's rewrite the general form of hole continuity equation 2.2 into a one-dimensional form

$$\frac{\partial p}{\partial t} = -\mu_h\frac{\partial p}{\partial x}E - \mu_h p\frac{\partial E}{\partial x} + D_h\frac{\partial^2 p}{\partial x^2} + (G_h - R_h), \tag{2.8}$$

where we used form for current hole density equation 2.3. By analogy for electrons we get

$$\frac{\partial n}{\partial t} = \mu_e\frac{\partial n}{\partial x}E + \mu_e n\frac{\partial E}{\partial x} + D_e\frac{\partial^2 n}{\partial x^2} + (G_e - R_e). \tag{2.9}$$

Next, we must consider the relationship between the electric voltage and the electric field. Voltage is defined as

$$U = -\int_{\mathbf{r}_A}^{\mathbf{r}_B}\mathbf{E}\cdot\mathrm{d}\mathbf{l}, \tag{2.10}$$

where the electric field increases from point $\mathbf{r}_A$ to some point $\mathbf{r}_B$ and $\mathbf{l}$ is an integration path.

2.3 Drift velocity

Let's rewrite the drift part in the drift-diffusion equations (2.2) and (2.6) in general form

$$\mathbf{j}_e = en\mu_e\mathbf{E} = en\mathbf{v}_e, \tag{2.11}$$

where we introduced

$$\mathbf{v}_e = \mu_e\mathbf{E} \tag{2.12}$$

the drift velocity of electrons. For holes, the situation is analogous.

2.4 Shockley-Ramo Theorem

If we have two infinite parallel electrodes at a distance L with a single electron between them, then according to [30] a hole moving with velocity v on the plates induces an instantaneous current

$$i(t) = \frac{ev(t)}{L}, \tag{2.13}$$

where e is the elementary charge. From the basic additivity of electrostatic charge based on Maxwell's equations, we get from the equation (2.13) the value of the instantaneous induced charge current Q between the electrodes

$$I(t) = \frac{Q(t)\, v(t)}{L}, \tag{2.14}$$

where we assume a charge moving with the same velocity v. Equation (2.14) is a special case of the Shockley-Ramo theorem which we choose because of the application to our model of the detector, which we define in the next section.

2.5 1D Detector Model Assumptions

For a simpler explanation of the observed phenomena, we will consider a rectangular detector with two planar contacts at distance L. The detector model is shown in figure 2.1. Next, we assume the size of the electrodes is much larger than the distance L. This assumption allows us to simplify spatial dimensions in the equations above to only one spatial dimension perpendicular to the contacts.

From the symmetry of the rectangular detector, we can say that the homogeneous electric field will be located between the centers of the electrodes. The laser spot with area S is small enough that the inhomogeneity of the electric field near the edges can be neglected. This can only be said if the electrodes are of the same size placed concentrically, which we further assume. Otherwise, the electric field will be at an angle to the electrodes, causing further inaccuracies. That is why we will illuminate the center of the contacts. In the experimental part of this paper, we will confirm this phenomenon by experiment.

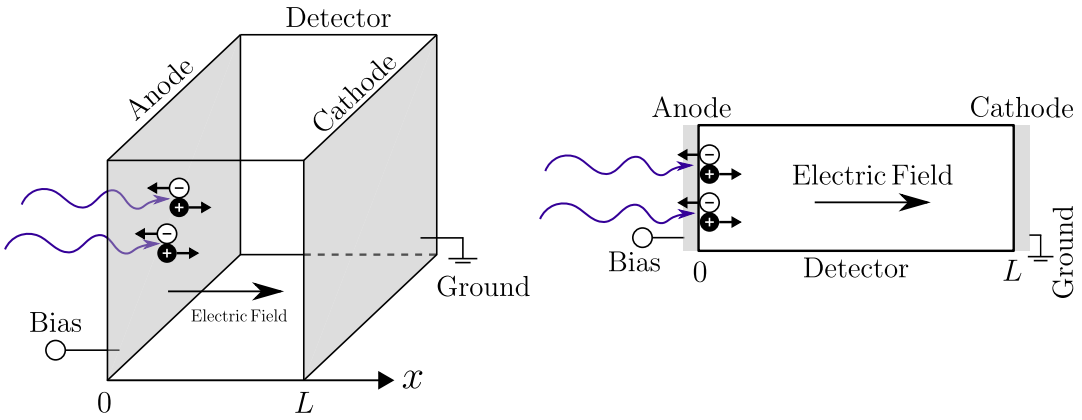

Figure 2.1: **Left:** General detector scheme with two metal electrodes painted with gray color. **Right:** One-dimension model of the detector with concentric contacts (gray color). Particles can move only along x-axis. The vertical axis of the detector is only used to facilitate the visualization of many photo-generated pairs. Electrons are represented by white circles and holes by black circles. The light from the left entering the anode is shown by the purple curved arrow.

A bias U is applied to the electrodes by an external generator. Photons are absorbed after hitting the detector. We use photons with energy greater than the band gap of our perovskite samples so photons are absorbed close to the surface.

The schematic is shown in figure 2.1. After the photon is absorbed, the electron-hole pair (also e-h pair) is created which splits due to the applied voltage and the individual free-charged carriers drift to the respective electrodes.

For generation e-h pairs we use a laser diode. We do not consider absorption on metal contacts and due to the low light beam intensities, the reflectivity of the contacts is also neglected. Free charge carriers moving through the detector starts to induce an electric current given by the equation (2.14) we are measuring. The characteristics of the measured current signal depend on the energy of the incident photons, the absorption coefficient and the magnitude of the generated charge, material dislocations, and more.

2.6 Optoelectronics Assumptions

From an optoelectronic point of view, we will assume that the drift mobility μ is space and time-independent. We will choose the such intensity of illumination that the photo-generated charge is small it does not affect the electric field created from the external voltage source - so the plasma effect is negligible. Next, we also assume that the applied electric field E is also time constant during the charge carrier transit. That is why we choose a laser pulse delay larger than $100\mu s$. Below $100\mu s$ seconds, the RLC phenomena occur in the circuit. Throughout this paper, we do not consider the mutual recombination of photogenerated electrons and holes. The total current is equal to the sum of the currents the electrons and from the holes, based on the charge additivity from Maxwell's equations. We do not consider the temperature change of the detector during the measurement.

3. Charge Distribution and Current Response

Now we turn to the actual theoretical description of the dependencies of the induced current. We try to model different situations of photon absorption using the charge density of the photogenerated charge, where by applying the Shockley-Ramo theorem we obtain the desired induced current curves. We also take into account different the finite lifetimes of the charge or different profiles of the electric field in the detector. In the last subsection, we describe the effect of recombination on the induced current during radiation absorption near the detector surface. Key are the assumptions we made in the previous chapter.

We use a laser diode with a wavelength of 450 nm throughout the measurement. Energy is larger than the $MAPbBr_3$ band gap so in the theoretical calculations, we expect that all photons are absorbed near the surface and that each photon generates an electron and a hole. According to the polarity, one particle is picked up by the electrode and the other type of particle starts to migrate through the detector to the other electrode. Drifting charge induces the current we measure. In this section, we will theoretically calculate the different types of the detector and how they affect the current responses.

3.1 Photon Flux

The photon flux is an important quantity in terms of determining the number of photo-generated charges contributing to photo-conductivity. According to [31], the photon flux is defined as

$$\Phi = H\frac{\lambda}{hc}, \tag{3.1}$$

where h is a Planck's constant, c is the speed of light, λ is the wavelength of the incident electromagnetic radiation and H is the area power density with unit $\left[\frac{W}{m^2}\right]$. The unit of the photon flux is $\left[\frac{\text{number of photons}}{m^2 s}\right]$.

3.2 Basic Drift

Let us first consider the simplest case, which is a constant charge density drifting across the detector in a constant electric field with no space charge nor generation-recombination processes. We start from the equation (2.8) that simplifies into the form

$$\frac{\partial p\left(x,t\right)}{\partial t} = -\mu_h \frac{\partial p\left(x,t\right)}{\partial x} E = -v_0 \frac{\partial p\left(x,t\right)}{\partial x}, \tag{3.2}$$

where the solution can written down with the initial charge distribution $p_0\left(x\right)$ as

$$p\left(x,t\right) = p_0\left(x - v_0 t\right). \tag{3.3}$$

This expression tells us, that the initial charge cloud moves with the constant velocity v_0. Using our detector in the figure 2.1 in $t = 0$ photo-generated hole

cloud is sharply localized under the anode $x = 0$ and

$$p_0(x) = N_0 \delta(x), \tag{3.4}$$

where N_0 is the initial number of free holes in the valence band (after surface recombination) and δ is the Dirac delta function. After including the time we get

$$p(x,t) = N_0 \delta(x - v_0 t)\, \chi_{[0,L]}(x). \tag{3.5}$$

Hole cloud center drifts from the anode ($x = 0$) to the cathode ($x = L$) with the constant velocity v_0. Let's define *transit time* by

$$\tau_{tr} = \frac{L}{v_0} = \frac{L}{\mu_h E} = \frac{L^2}{\mu_h U}, \tag{3.6}$$

with applied voltage $U = EL$. In other senses, we will mean by the term *transit time* the time when the center of the general hole bulk passed through the detector.

Total charge from the concentration equation (3.5) is set

$$Q(t) = e \int p(x,t)\, \mathrm{d}x \tag{3.7}$$

with (3.5) we get

$$Q(t) = Q_0 \chi_{[0,\,\tau_{tr}]}(t), \tag{3.8}$$

where $Q_0 = eN_0$ is the charge after the surface recombination (see section 3.7). The box car function represents charge drift from the anode until the bulk reaches the cathode. Applied the Shockley-Ramo theorem (2.14) on the previous equation we get time dependence of the induced current

$$I(t) = \frac{Q_0}{\tau_{tr}} \chi_{[0,\,\tau_{tr}]}(t) = I_0 \chi_{[0,\,\tau_{tr}]}(t). \tag{3.9}$$

This equation tells us that the current waveform of the rectangle with the height of $I = \frac{Q_0}{\tau_{tr}}$, see the figure 3.1. As can be seen, the charge cloud was approximated by a Gaussian curve because the Dirac delta in equation (3.4) is not physically possible in this case.

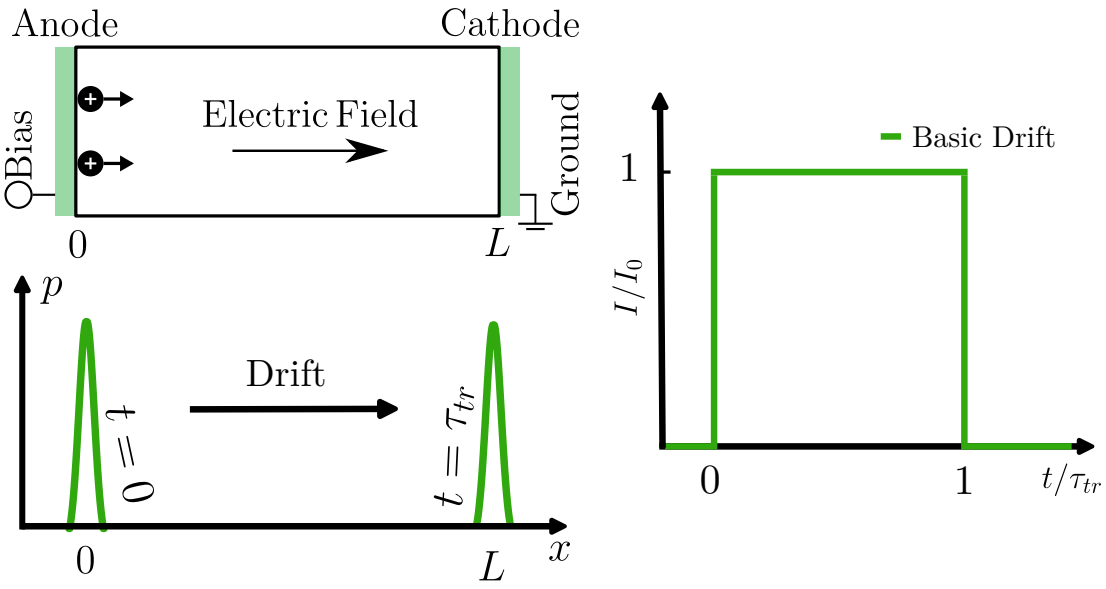

Figure 3.1: **Left Top:** Scheme of the detector and the hole cloud drifting towards the cathode with velocity $v = \mu_h E$. **Left Bottom:** Hole concentration represented by Gaussian approximation curve. **Right:** Normalized current WF via Shockley-Ramo theorem.

3.3 Charge Trapping on Traps

The quality of semiconductor detectors is strongly influenced by the number of locations (traps) where the moving charge can be caught. These traps reduce the efficiency of charge collection in the detector. The trapped charge has a higher probability of reverse thermal emission into the conduction (valence) band than recombination with the opposite charge trapped by the same center [32]. Assuming a uniform distribution of capture centers throughout the detector, the average time during which a charge is free before it is captured by a random center can be defined as τ_T - *trapping time*. In contrast, let us define the average time τ_D - *detrapping time*, during which the charge is trapped. Thus, according to [33] we can defined

$$\tau_T = \frac{1}{N_T \sigma_c v_{vh}} \quad \text{and} \quad \tau_D = \frac{1}{N_C \sigma_c v_{vh}} \exp\left(\frac{E_T}{k_B T}\right), \tag{3.10}$$

where N_T density of detention centers, E_T is their energy in the band structure, N_C denotes the effective density of states in the valence band, σ_c is the effective capture cross-section charge carriers, v_{vh} is the thermal velocity of the free carriers, T is the absolute temperature and k_B is the Boltzmann constant. The effect of traps on the current response shown in figure 3.2 can be divided into three basic cases.

In the first case, where the trapping time is much larger than the transit time $\tau_T \gg \tau_{tr}$, the traps do not affect the charge carriers and therefore the current response of the charge generated at the detector surface is given by (3.9) remains unchanged (fig. 3.2a).

3.3.1 Deep Trap

When the trapping time is comparable to the transit time $\tau_T \approx \tau_{tr}$ and the detrapping time is much longer than the transit time $\tau_D \gg \tau_{tr}$ and the trapping time $\tau_D \gg \tau_T$ at the same time, trapping occurs but not the recoil release of charge carriers during the transit time (fig. 3.2b). According to [33], the current response can be described as follows

$$I(t) = \begin{cases} 0 & \tau_{tr} < t \\ \frac{Q_0}{\tau_{tr}} \exp\left(-\frac{t}{\tau_T}\right) & 0 \leq t \leq \tau_{tr} \end{cases} \tag{3.11}$$

3.3.2 Shallow Trap

When the release time from the trap τ_D is also comparable to the time of the charge passage ($\tau_T \leq \tau_{tr}, \tau_D \leq \tau_{tr}$), transit time is not unambiguously determinable! For time $t > \tau_{tr}$ some holes can be collected on the detector cathode. Analytical solution of the system of differential equations describing the shallow trap does not exist [34] and therefore Monte Carlo simulation must be used for current waveform analysis. For this reason, the drift mobility (2.1) must be reduced, which let's call the effective drift mobility μ_{eff}. Consider the trapping time τ_T when the hole is free to drift in the sample with the mobility μ_h and detrapping time τ_D when the hole is trapped and cannot drift. So we get effective mobility

$$\mu_{\text{eff}} = \mu_h \frac{\tau_T}{\tau_T + \tau_D}, \tag{3.12}$$

where the transit time is prolonged

$$\tau'_{tr} = \tau_{tr} \frac{\tau_T + \tau_D}{\tau_T}. \tag{3.13}$$

Let us note that the mobility-lifetime product remains unchanged in this case, as it is apparent from equation (3.12) and (3.13).

3.3.3 One Shallow and One Deep Trap Model Notation

Let's define two types of traps. *Shallow trap* - the charge is captured and thermally released in times smaller than the detector transit time. These times, let us denote τ_{TS} and τ_{DS}, respectively. The trapping and release processes that occur during the drift can be repeated arbitrarily. *Deep trap* - a trap with trapping time τ_{TD} and thermal emission time τ_{DD} longer than the charge transit time through the detector τ_{tr}, so back-release into the valence band is unlikely and will be neglected in further calculations. A schematic of the charge capture and release on the traps is shown in figure 3.2c.

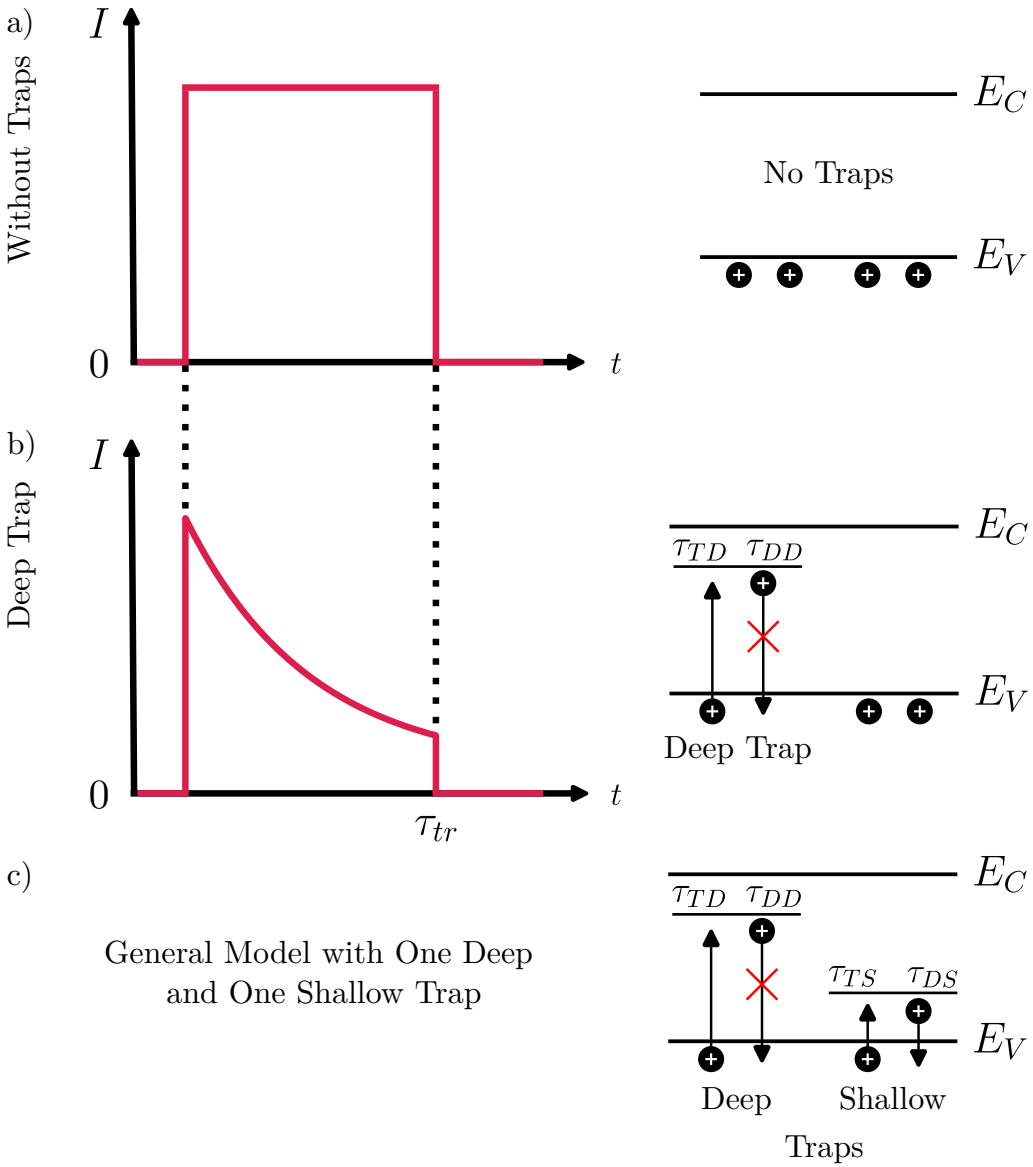

Figure 3.2: Possible shapes of the current response of the charge generated at the detector surface obtained by the TOF method **Top:** without traps; **Middle:** with a deep trap; **Bottom:** with the possibility of capture and release with times τ_T, τ_D much smaller than the time τ_{tr}. Redrawn from [33].

3.4 Electric Field

A fundamental problem with radiation detectors is the strong dependence of the Charge Collection Efficiency (CCE) (see section 3.8) on the electrical field profile inside the detector. The measured induced current according to (2.14) depends on the magnitude of the charge moving between the electrodes and in the case of material inhomogeneities or defects, only part of the photo-generated charge may be used. The generation of a secondary electric field by the accumulation of space charge acting against the original electric field results in the creation of a space within the detector with reduced or zero electric fields where no charge can move. This significantly degrades the detection properties of the used detectors.

So far we have considered a constant electric field along the entire length of the detector. Now we derive the dependence of the induced current for situations where we assume charge accumulation - polarization of the detector.

3.4.1 Constant Space Charge

Let us assume a constant charge density $\rho(x) = \rho_0$ along the length of the detector. We solve the electric field profile $E(x)$ from the Gauss law

$$\oint \mathbf{D} \cdot \mathrm{d}\mathbf{S} = Q_{in}, \tag{3.14}$$

where $\mathbf{D} = \varepsilon_r \varepsilon_0 \mathbf{E}$ is the electric displacement field, ε_0 is the vacuum permittivity, ε_r is the relative permittivity of the used material and Q_{in} is the charge enclosed by the integration surface $\mathbf{S}$. Thus, consider the Gaussian surface formed by the cuboid in our model in figure 3.3 bounded on the side by surfaces at distances $-b$ and b from the center of the detector. The intensity vector is parallel to the cube shell and therefore the intensity flux through the shell is zero.

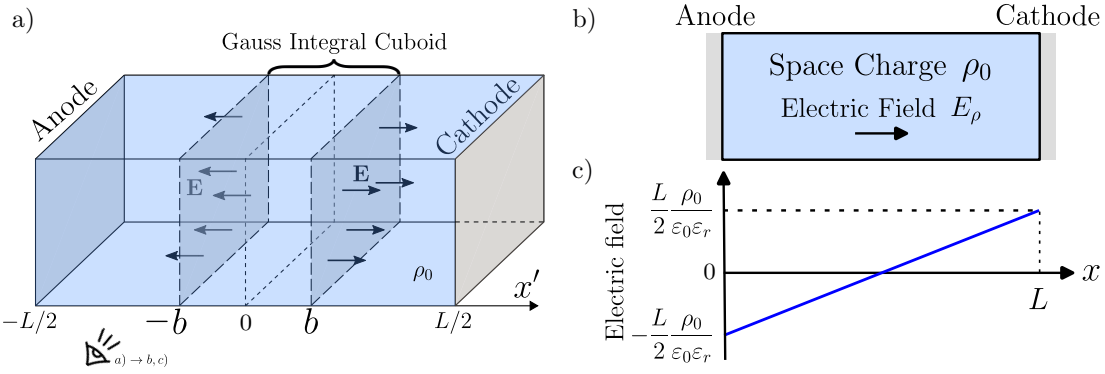

Figure 3.3: Gaussian surface (cuboid) is marked in our detector model. A rectangular cuboid is bounded on the side by the detector boundary. And inside the detector, the boundaries are squares at distances $-b$ and b from the center of the detector. The areas have content S. The whole detector contains the charge density ρ_0.

On the other hand, the intensity vector has the same magnitude at all points of the base and is perpendicular to it (and therefore parallel to the normal vector), so we can simplify the scalar product (3.14)

$$\oint \mathbf{E} \cdot \mathbf{n} \mathrm{d}S = 2SE(b), \tag{3.15}$$

where b is a length parameter. By substituting into the equation (3.14) and considering the right side $Q_{in} = 2bS\rho_0$, we get

$$E_\rho(b) = b\frac{\rho_0}{\varepsilon_0\varepsilon_r}. \tag{3.16}$$

Applied to our x coordinates model, figure 3.3b,c we finally obtain the dependence of the electric field created by constant space charge

$$E_\rho(x) = \frac{\rho_0}{\varepsilon_0\varepsilon_r}\left(x - \frac{L}{2}\right) = a\left(x - \frac{L}{2}\right), \tag{3.17}$$

where we have marked slope $a = \frac{\rho_0}{\varepsilon_0\varepsilon_r}$.

3.4.2 Linear Electric Field

From electrostatic additivity, the resulting electric field inside the detector must consist of the charge density electric field E_ρ and the electric field generated by the external source E_{ext} and since we have an electric field only in the direction of the detector length we can write non-vector

$$E = E_{ext} + E_\rho, \tag{3.18}$$

so

$$E = E_0 + a\left(x - \frac{L}{2}\right) \tag{3.19}$$

where we used bias voltage $E_0 = \frac{U}{L}$. Figure 3.4 shows the basic possibilities of the electric field as a function of the space charge density ρ_0. When no space charge

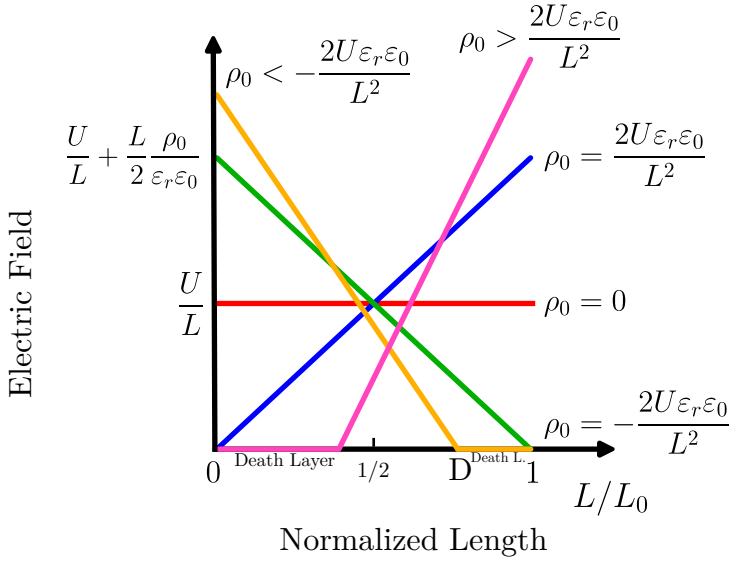

Figure 3.4: Electric field profiles

is present we get a constant electric field only created by the external source (red line). Initial constant space charge in the detector cannot be sustained without applied bias (U = 0) at equilibrium and is neutralized [33]. Further, the greater the space charge the greater the tilt of the initially constant electric field depending on the applied voltage (blue and green curves). There may also be

a situation when the electric field of the space charge becomes greater than the electric field of the external source - *dead layer* is created. The inactive layer is a region inside the detector where the electric field is almost zero (required from the continuity equation). The dead layer coordinate of zero electric fields from figure 3.4 starts at

$$D\left(\rho_0\right) = \frac{L}{2} - \frac{E_0}{a}. \tag{3.20}$$

The space charge in the dead layer is filled with the free charge so the equation (3.18) transforms to

$$E\left(x\right) = \max\left(0,\, E_0 + a\left(x - \frac{L}{2}\right)\right). \tag{3.21}$$

The current WFs we derive from the general kinetic differential equation

$$v\left(t\right) = \dot{x}\left(t\right) = \mu_h E\left(x\left(t\right)\right). \tag{3.22}$$

Reached

$$\dot{x}\left(t\right) = \mu_h\left(E_0 + a\left(x - \frac{L}{2}\right)\right). \tag{3.23}$$

By integral separation with boundary condition $x\left(0\right) = 0$ we get solution

$$x\left(t\right) = \left(E_0 - \frac{La}{2}\right)\frac{e^{a\mu t}}{a} - \frac{E_0}{a} + \frac{L}{2}, \tag{3.24}$$

where $a = \frac{\rho_0}{\varepsilon_0\varepsilon_r}$. Velocity is obtained by time derivative

$$\frac{\mathrm{d}x}{\mathrm{d}t} = v\left(t\right) = \mu\left(E_0 - \frac{La}{2}\right)e^{a\mu t}. \tag{3.25}$$

So finally, time dependence of the hole current waveforms is

$$I\left(t\right) = \frac{Q\left(t\right)v\left(t\right)}{L} = \frac{Q_0}{L}\mu\left(E_0 - \frac{La}{2}\right)e^{a\mu t}, \tag{3.26}$$

where we didn't anticipate any trapping so total drifting charge has constant value $Q\left(t\right) = Q_0$. Transit time is simply derived from equation (3.24) $\left(x\left(t\right) = 0\right)$

$$\tau_{\mathrm{tr}}\left(a\right) = \frac{1}{\mu a}\ln\left(\frac{2E_0 + aL}{2E_0 - aL}\right) = \frac{1}{\mu a}\ln\left(\frac{1 + \frac{a}{A}}{1 - \frac{a}{A}}\right), \tag{3.27}$$

where $A = \frac{2U}{L^2}$ is the slope of the electric field for which the inactive layer starts to form. All electric field options and their current responses are shown in figure 3.5. It is interesting to note the extreme case for $a = A$ where the transit time is at infinity and the current waveform is just a decreasing exponential.

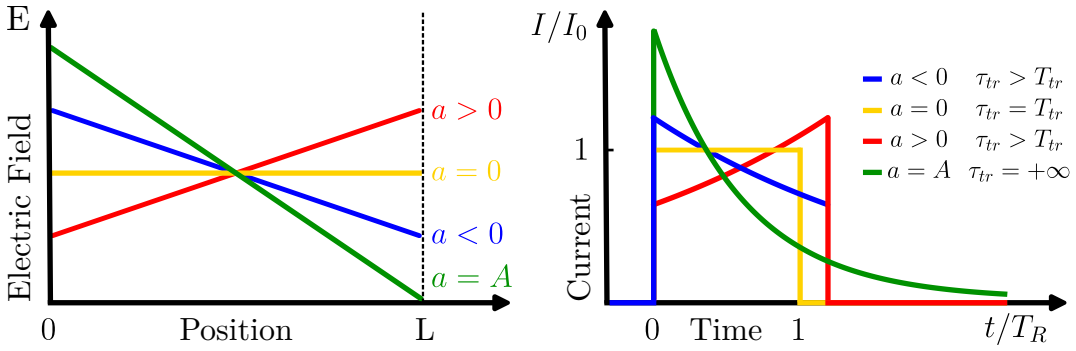

Figure 3.5: **Left:** Electric field depending on slope a. **Right:** Normalized current waveforms.

3.5 Leading Edges

What happens when the whole delta charge cloud starts drifting at almost the same time, we have already presented in Chapter 3.2. The initial bulk can be modelled by the Dirac delta function δ. We now look at other more realistic leading edges of current waveforms. All the following examples consider a constant electric field at the beginning of the detector.

3.5.1 Constant Charge

We first derive the case where the photogenerated charge enters the detector in the same amount, so the amount of charge entering the detector is

$$\frac{\mathrm{d}Q}{\mathrm{d}t} = \frac{Q_0}{t_0} = \text{konst.}, \tag{3.28}$$

where t_0 is the time when the last standing charge began to drift. By integration, we get the time dependence of the amount of drifting charge on time

$$Q\left(t\right) = \frac{t}{t_0} Q_0. \tag{3.29}$$

The dependence is valid only for $0 \leq t \leq t_0$. Then all the charge drifts through the detector. The situation for the constant bulk is shown in figure 3.6. The induced current is simply linear.

3.5.2 Gaussian Charge

Another more realistic case is the gaussian-shaped bulk (delta bulk approximation). So let's have a normalized Gaussian cloud

$$\frac{\mathrm{d}Q}{\mathrm{d}t} = \frac{Q_0}{\sqrt{\pi}} e^{-t^2} \tag{3.30}$$

where after integration we get the dependence of the amount of drifting charge on time

$$Q\left(t\right) = \frac{Q_0}{2} \mathrm{erf}\left(t\right). \tag{3.31}$$

erf (t) is the error function. Both charge and current dependencies are plotted in figure 3.7.

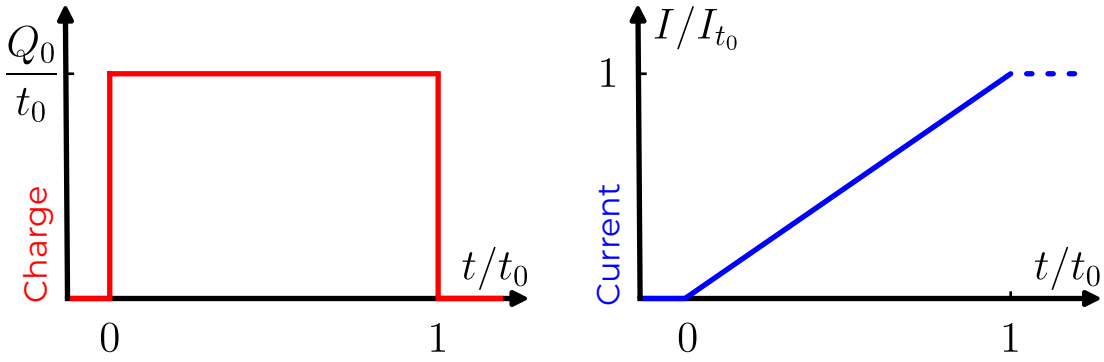

Figure 3.6: **Left:** Time dependence of the amount of charge entering the detector volume. **Right:** Current response dependencies for constant charge.

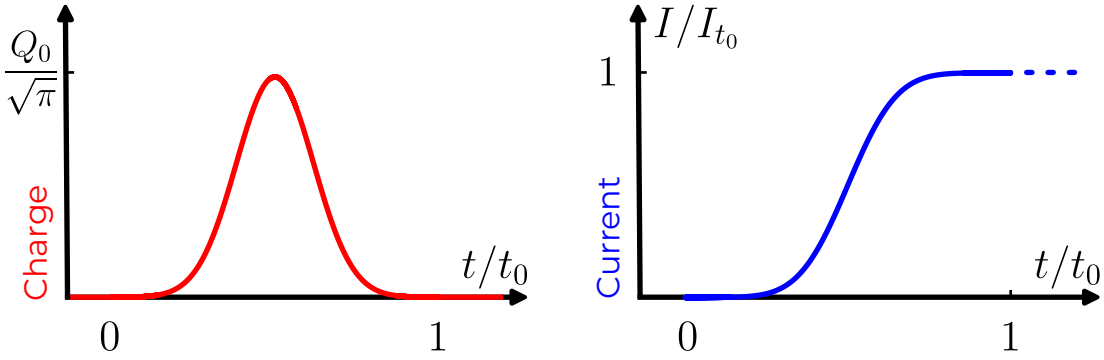

Figure 3.7: **Left:** Time dependence of the amount of charge entering the detector volume. **Right:** Current response dependencies for gaussian charge.

3.5.3 Triangle Charge

Let's choose a triangular edge as the next leading edge. The triangle function is defined as

$$\frac{\mathrm{d}Q}{\mathrm{d}t} = \mathrm{tri}\,(t) = \begin{cases} Q_0\,(1-|t|)\,, & |t|<1; \\ 0 & \text{otherwise.} \end{cases} \tag{3.32}$$

and its time dependence on the amount of drifting charge

$$Q\,(t) = -\frac{t\,|t| - 2t - 1}{2} Q_0. \tag{3.33}$$

Both, the charge and its current dependencies are shown in figure 3.8.

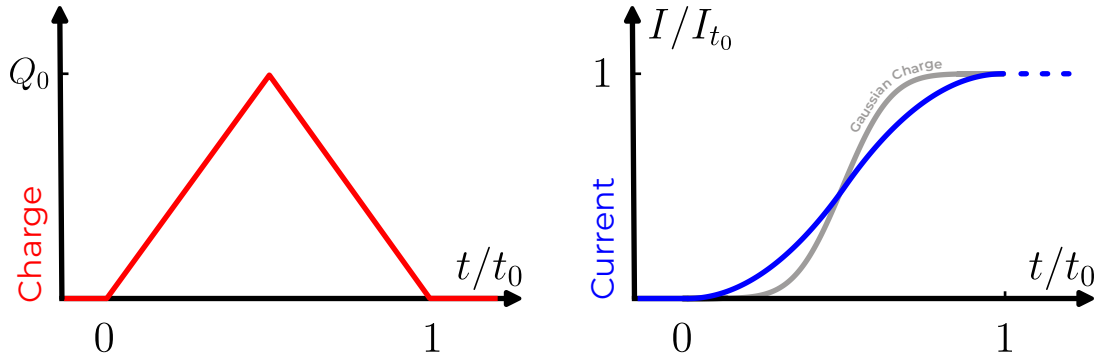

Figure 3.8: **Left:** Time dependence of the amount of charge entering the detector volume. **Right:** Current response dependencies for triangle charge. The grey curve is a current response for Gaussian charge from figure 3.7.

3.5.4 Log-normal Charge

And last we calculate the current response of the basic log-normal distribution

$$\frac{\mathrm{d}Q}{\mathrm{d}t} = \frac{Q_0}{t\sqrt{\pi}} e^{-\ln^2 t}. \tag{3.34}$$

By integration we again obtain the time dependence of the amount of drifting charge through the detector

$$Q\left(t\right) = \frac{\mathrm{erf}\left(\ln\left(x\right)\right)}{2} Q_0. \tag{3.35}$$

The waveforms of both charge and induced current are shown in figure 3.9.

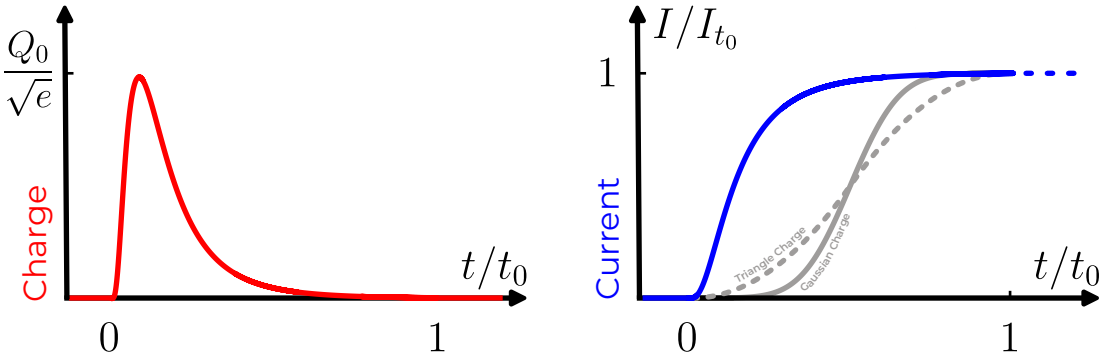

Figure 3.9: **Left:** Time dependence of the amount of charge entering the detector volume. **Right:** Current response dependencies for log-normal charge. The grey curves are the current response from figure 3.7 and 3.8.

3.6 Diffusion

Until now, we've neglected the diffusion coefficient D in drift-diffusion equations. So let's consider non-zero hole diffusion $D_h \neq 0$ and again neglect generation-combination processes $GR = 0$ with a constant electric field $\frac{\partial E}{\partial x} = 0$. 1D form of holes equation (2.8) gives us

$$\frac{\partial p}{\partial t} = -\mu_h E \frac{\partial p}{\partial x} + D_h \frac{\partial^2 p}{\partial x^2}. \tag{3.36}$$

This equation is a special case of the Einstein-Kolmogorov equation for Brownian motion with constant diffusion coefficient and drift velocity [35]. Applied to the basic constant electric field drifting charge from the section 3.2 we get [36]

$$I(t) = \frac{Q_0}{\tau_{tr}} \Theta(t) \frac{1}{\sqrt{4\pi D_h t}} \int_0^L \exp\left(-\frac{(x - v_h t)^2}{4 D_h t}\right) \mathrm{d}x. \tag{3.37}$$

The diffusion process is shown in figure 3.10. Photons create a hole cloud that moves towards the opposite negative electrode with the velocity $v_0 = \mu_h E$. During movement, the cloud starts to expand both into and against the direction of movement, but the centre remains the same and is not affected by the diffusion. As shown in the theoretical model the hole cloud expands in the shape of a gaussian (left plot). Diffusion smears the transient edge (right plot).

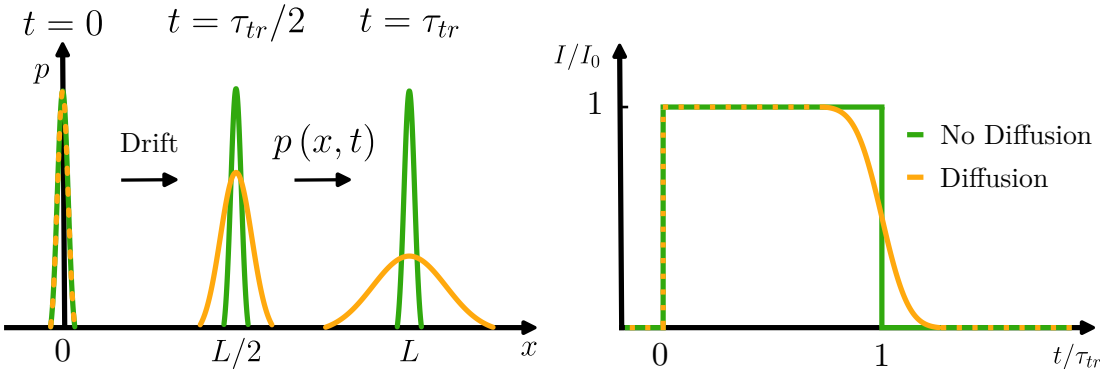

Figure 3.10: **Left:** Evolution of the hole cloud concentration $p(x,t)$. **Right:** Normalized current WFs of the detector with (orange curve) or without (green curve) the diffusion.

3.7 Surface Recombination

After the beam hits the semiconductor detector and creates e-h pairs close to the surface at a depth much shorter than the length of the detector, surface recombination (SR) can occur. Consider a detector like the one in the picture 3.11 with a length of L. The surface recombination is characterized by the surface recombination velocity s, which defines the probability p_{bulk} of charge entering from the surface layer to the bulk [37]. Based on the formula

$$\frac{p_{\text{bulk}}}{1-p_{\text{bulk}}} = \frac{v}{s}, \tag{3.38}$$

where v is the charge drift velocity. By expressing p_{bulk}

$$p_{\text{bulk}} = \frac{1}{1+\frac{s}{v}} \tag{3.39}$$

and substituting $v = \mu E = \mu \frac{U}{L}$ considering constant electric field we get

$$p_{\text{bulk}} = \frac{1}{1+\frac{sL}{U\mu}}. \tag{3.40}$$

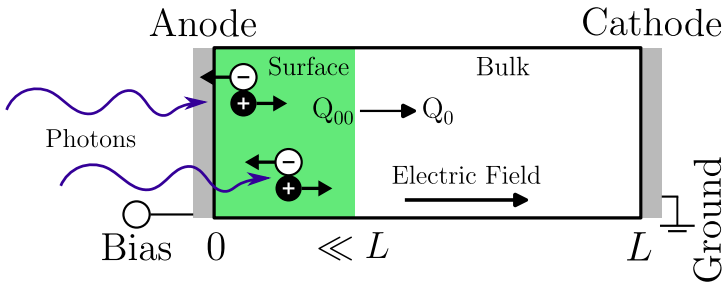

Figure 3.11: Schematic of surface recombination in a detector with bulk and surface layer. Photogenerated charge Q_{00} partially recombine and rest charge Q_0 enters the bulk. Holes are black positive and electrons are white negative dots. Photons are marked with purple curved arrows.

Amount of the photo-generated charge Q_{00} will partially recombine to the amount of Q_0, so (3.38) can be finally rewritten as

$$Q_0 = Q_{00}\frac{1}{1+\frac{sL}{\mu U}}. \tag{3.41}$$

So in all the current waveforms, we have already derived, we calculated the charge after the surface recombination Q_0. The effect of surface recombination on current waveforms can be seen in figure 3.12. When we normalize the curves without surface recombination by the applied voltage (Fig.3.12 **Bottom** plots), we get overlapping curves (Fig.3.12 **Left Bottom**). On the other hand, surface voltage causes a slight current drop, so the bias normalized current WFs start to have a slight shift (Fig.3.12 **Right Bottom**).

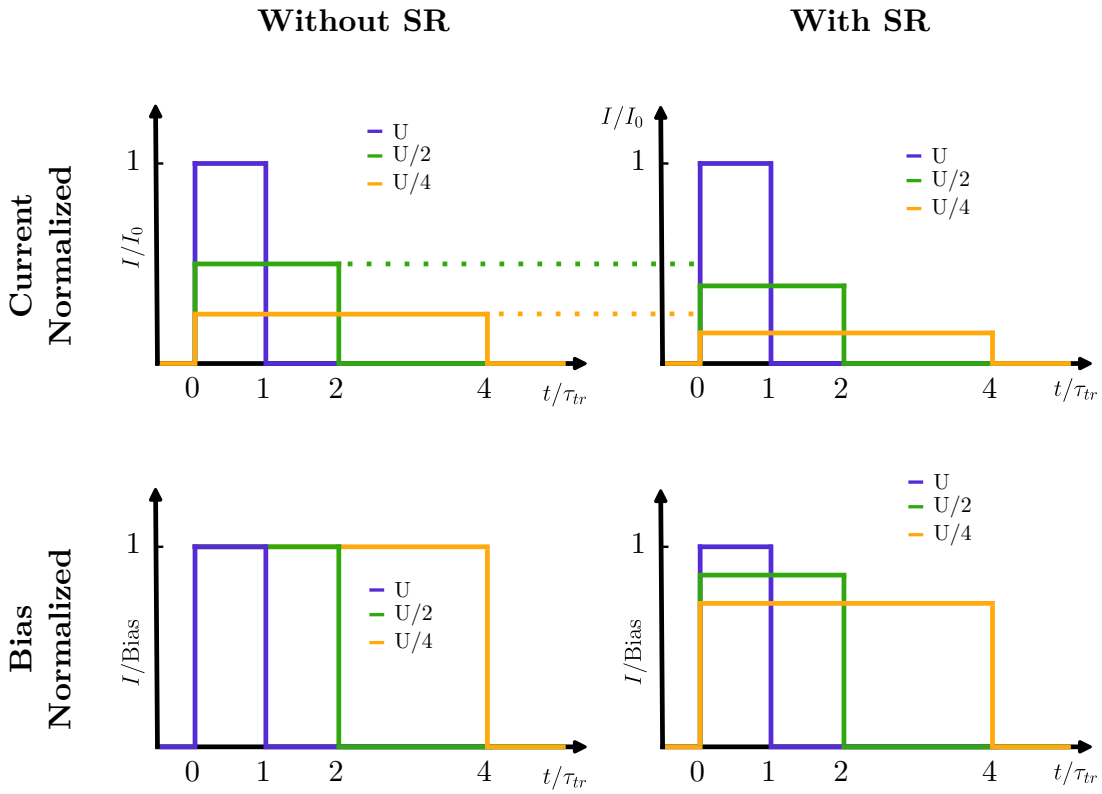

Figure 3.12: U is the applied bias. **Left Top:** Current WFs for the detector without surface recombination. **Right Top:** Current WFs for the detector with surface recombination. **Left Bottom:** Biased current WFs for the detector without surface recombination. **Right Bottom:** Biased current WFs for the detector with surface recombination.

3.8 Charge Collection Efficiency

One of the most important parameters evaluating radiation detector quality is called *Charge collection efficiency* (CCE) and is defined as a fraction of the collected charge to the generated charge. As a simple example of a deep trap, we can derive [38] from the Hecht equation

$$\mathrm{CCE} = \frac{\tau_T}{\tau_{tr}} \left[1 - \exp\left(-\frac{\tau_{tr}}{\tau_T}\right)\right], \tag{3.42}$$

where τ_T is trapping time and τ_{tr} is transit time. Including surface recombination, we get [39]

$$\mathrm{CCE} = \frac{\tau_T}{\tau_{tr}} \frac{1}{1 + \frac{s}{v}} \left[1 - \exp\left(-\frac{\tau_{tr}}{\tau_T}\right)\right], \tag{3.43}$$

where s is the surface recombination velocity and v is the charge drift velocity.

4. Experiment

4.1 Bipolar and Continuous DC Regime L-TCT

L-TCT can be divided into two modes according to the time course of the applied bias - *Continuous* DC and *Bipolar* DC. In the first case, a continuous DC bias is applied to the detector, which is not related to the time course of the detector illumination. The incident electromagnetic radiation generates a photo-charge which, during its migration to the appropriate electrode may be trapped in various locations in the detector. The internal electric field generated by the external source is modified by the continuously accumulating charge. We are talking about the polarization of the detector. Polarization can also be caused by impurities or non-ideal crystal structures.

In contrast, the bipolar DC mode consists of a time-varying DC bias that is time-locked to the laser pulse according to the diagram in figure 4.1. The pulsing scheme is defined by the pulse period T, the width of the first bias pulse $T+$, the width of the second opposite polarity bias pulse $T-$ and the laser pulse delay LPD after the first bias pulse is turned on. And of course the magnitude of the bias pulses $U+$ and $U-$. A suitable choice of these parameters can achieve a measurement configuration where the above-mentioned polarization of the detector is suppressed.

Our main aim is to describe the behaviour of photo-generated carriers (electron - hole pairs) where other disruptive elements could be ideally neglected. We think of perovskite ions [29]. If only DC bias is applied charged ions start to drift through the bulk to the oppositely charged electrodes and so the disruption of the internal electric field is possible. So that is why the bipolar regime is used, to prevent from the drift of charge (ions) at electrodes. Bipolar bias should hold the centre of drifting ions at the same place. The schema of the bias and laser pulses is shown in figure 4.1.

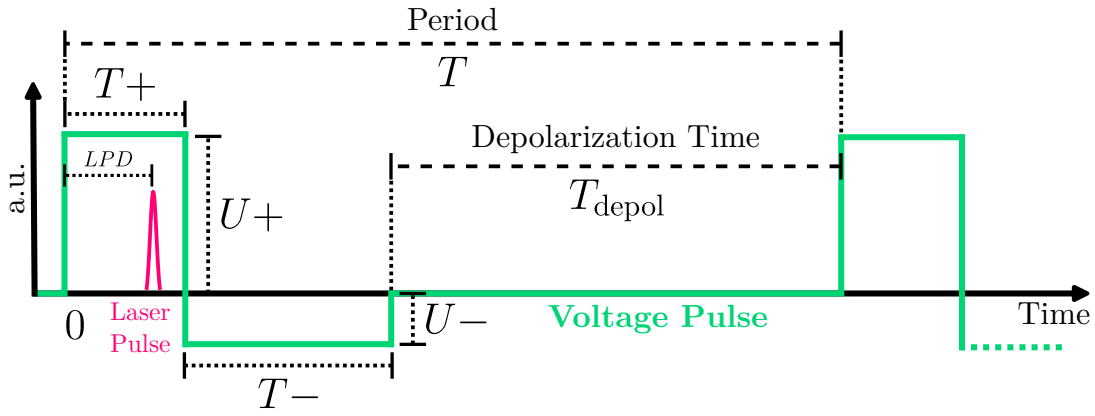

Figure 4.1: Schema of the bias and laser pulses for the bipolar L-TCT.

4.2 Aparatus

Our apparatus, shown in figure 4.3, consists of three types of components. Electric devices are marked with blue rectangles, optical components are shown by pictograms and the perovskite detector with shielding is visualized by schematic picture.

The heart component of our L-TCT setup is an arbitrary voltage function generator *Tektronix AFG31000*. We generate time-dependent arbitrary voltage waveforms according to the scheme in figure 4.1. Generated voltage pulse enters *WMA-300 Falco Systems* High speed high voltage amplifier with 50x amplification and continues straight on the perovskite detector. The second voltage output from the arbitrary generator is connected to the pulse generator *Picosecond Pulse Labs* model 10.070A which triggers the laser diode.

Detector photo-current response is so weak it has to be amplified by current amplifier. We use a custom-made 730x amplifier. Distortion cause by amplifier is shown in figure 4.2. The signal amplifier is directly connected to the oscilloscope *LeCroy WaveRunner 6Zi*. There is also a trigger connection from the picosecond generator to the oscilloscope for the purpose to synchronize all pulsing electronics parts.

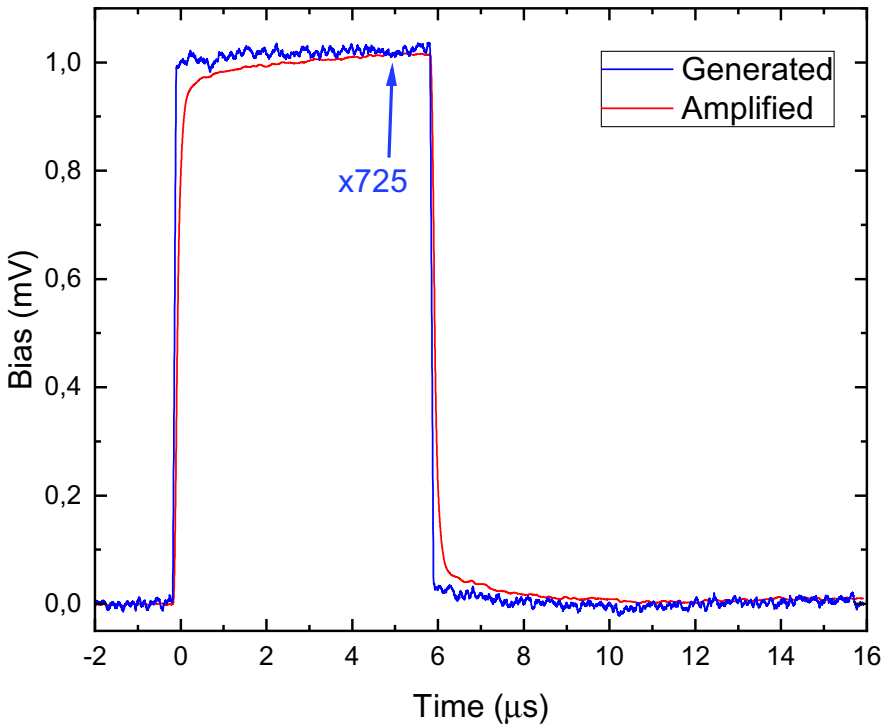

Figure 4.2: $6\mu s$ 1V rectangular bias pulse from arbitrary voltage generator Tektronix AFG31000 amplified by custom-made 730x amplifier both directly measured with oscilloscope. The amplifier clearly smooths the edges.

PC-controlled shutter is used to block laser pulses for measurement of the background (dark) current which is then subtracted from shutter-opened measurement. So we get clear photo-current waveforms without background distortion.

And to be consistent in the collected charge for every single sample measure-

ment we use a neutral density (ND) filter to attenuate laser diode intensity. The filter is provided with scale.

The laser beam 1 μs pulses are focused at the centre of the detector forming approximately 1 mm^2 spot. As an above band-gap light source we use laser diode with wavelength $\alpha = 450$ nm. A laser diode is triggered by a picosecond generator with a possible repetition rate 1 Hz $-$ 100 kHz. Laser pulse delay after the rise of voltage pulse can be set to avoid the formation of space charge inside the detector.

The oscilloscope, arbitrary voltage function generator and shutter are controlled by a computer which allows us to automate the whole measuring process.

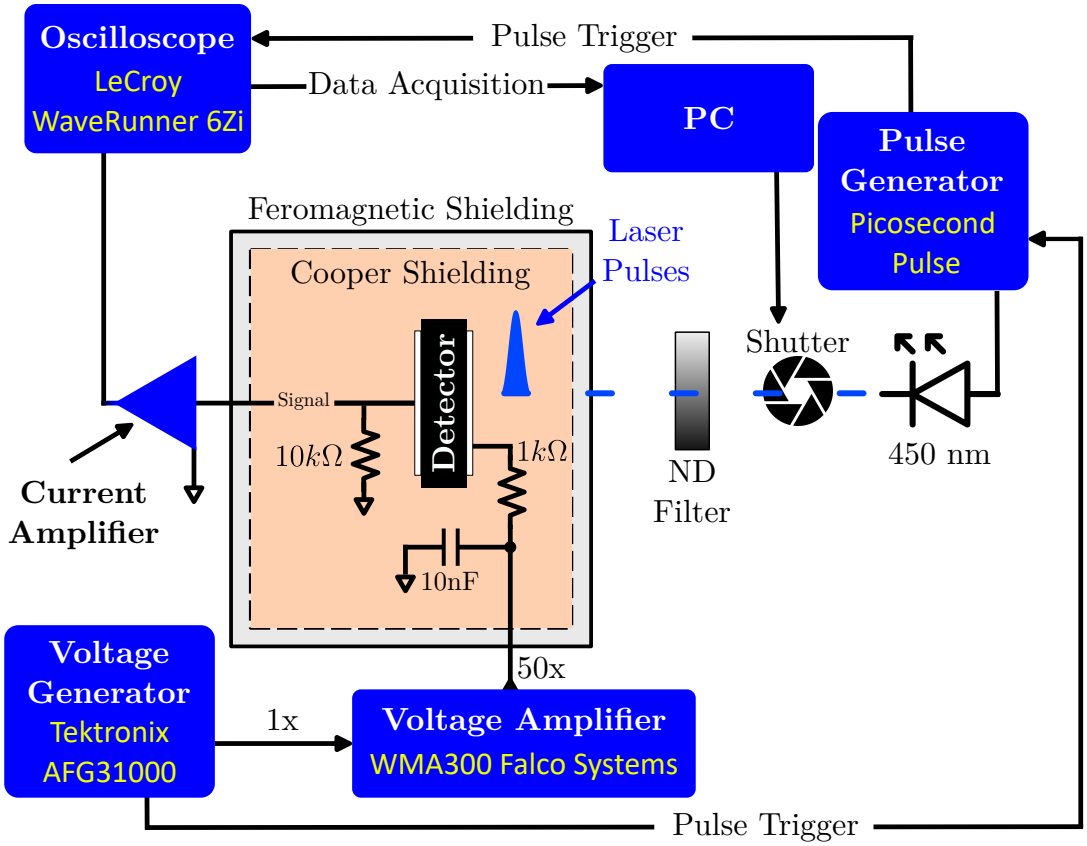

Figure 4.3: Schema of our L-TCT setup.

4.3 Current Waveform

The pulsing scheme shown in figure 4.1 is highly idealized. In real equipment, due to the steep leading edge of the applied voltage pulse, relaxation to the required values occurs only after a certain time due to RLC phenomena in the electrical circuit. All time parameters selected T, $T+$, $T-$, LPD, are deliberately chosen to respect the condition of a non-polarized detector and at the same time to come as close as possible to the idealization of pulsation according to the scheme in figure 4.1.

To clarify the choice of pulsing parameters, we measured the time course of the current in the detector, as well as the triggering and voltage pulse, using an oscilloscope. The trigger pulse is directly connected to the oscilloscope. Figure

4.4 shows all the signals on one timeline. After switching on the voltage it is necessary to wait for at least $80\mu s$ for the voltage to reach the desired value. The incoming light pulse generating a photo-charge will affect the conductivity of the semiconductor detector. This change is reflected by a voltage deviation from the dark voltage. By subtracting the voltage response from the background voltage we get the time dependence of the voltage induced by the photo-generated charge. The current values are obtained by recalculating the voltage using the amplifier resistance and the input resistance of the oscilloscope. The current induced by electrons or holes takes different signs depending on the inducing charge and the polarity of the applied voltage.

Let's have a convention, that will display the main part of the subtracted current response from the current RLC background to positive values. The time dependence of the measured current after subtraction background current without a light pulse, applying the convention just mentioned we will call the current waveform (WF for short).

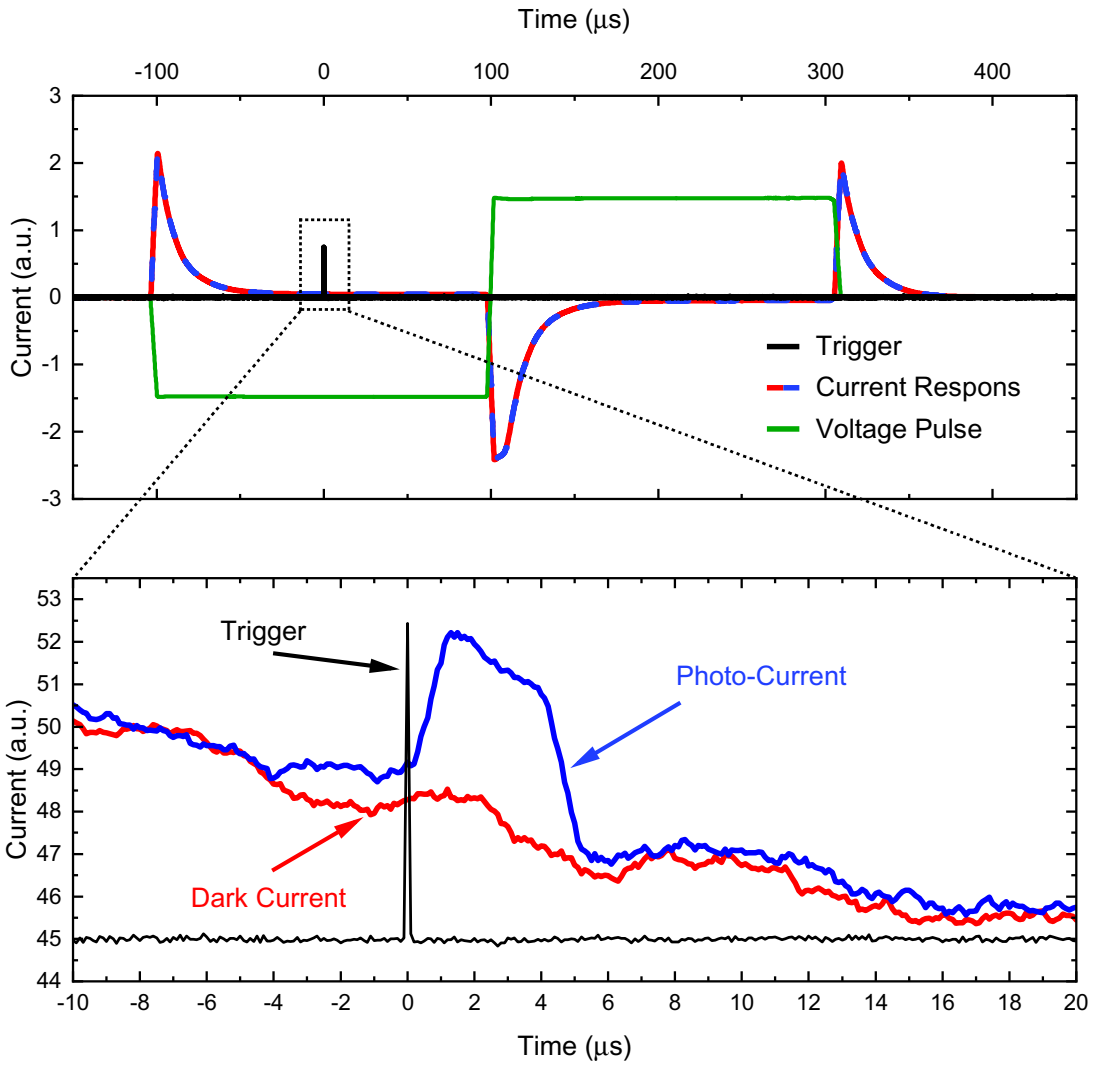

Figure 4.4: **Top:** Trigger pulse, the voltage pulse of the external voltage source and the current between detector contacts. **Bottom:** Detail of the upper image in the interval from $-10\,\mu$s to $20\,\mu$s. Arbitrary current units. Our waveform is obtained by subtracting Current Response and Dark Current.

4.4 Monte Carlo Simulation

The theoretical calculation of current responses based on the current continuity equation is analytically solvable only for a detector containing a single trap [34]. The derived current dependence relations in the previous chapter do not include the possibility of backward release of the trapped charge - shallow traps. Therefore, in the interpretation of the measured data, we use a Monte Carlo numerical simulation (abbr. MC), where this phenomenon can be included [34, 40]. The method used works with a two-level detector model of one shallow and one deep trap. The detailed mechanism of the method used can be found in the thesis [36] of J. Pipek.

4.5 Samples

4.5.1 Technical Overview

We use two methylammonium lead tribromide samples. Detectors are prepared at a research institute for electronics and information technologies *CEA-Leti* and at *Université Grenoble Alpes*. Both institutions are located in Grenoble, France. Samples were already equipped with chromium contacts. We glued the samples to the printed circuit board with a non-conductive adhesive and applied a contact wire glued with graphite conductive paste to the corner of the contacts. All technical details are summarized in table 4.1. The real sample is a view in the figure 4.5.

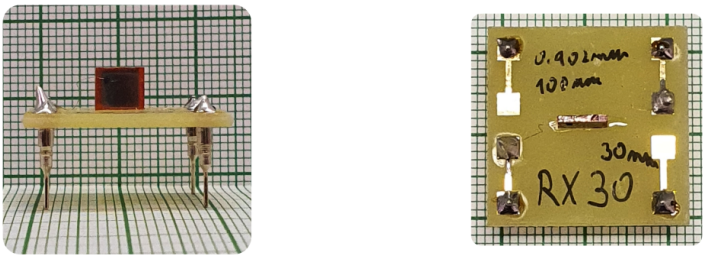

Front View Top View

Figure 4.5: RX30 sample (orange colour) glued to a printed circuit board (yellow dark colour) with contacts (gold reflective colour).

Table 4.1: Summary of our samples. The contact column tells us the contact material and the thickness of the contacts on the front and back side.

Name	Material	Size	Contacts	Made by
RX23	$MAPbBr_3$	$5 \times 4.5 \times 0.69\,mm$	Cr 30/100nm	CEA-Leti and
RX30	$MAPbBr_3$	$5 \times 5 \times 0.9\,mm$	Cr 30/100nm	Uni Grenoble

4.5.2 Spacial Homogeneity

We want to be sure that the measurement results are independent of the light beam position on the detector so the samples are homogeneous. We divided the detector into five equally distributed sections according to the diagram shown in figure 4.6. We shine only on the contact because outside of it we are predicting an inhomogeneous electric field and indescribable phenomena caused by defects from the sample preparation itself.

After a short repetitive measurement at each of the five points on the detector, it was found that random phenomena occur at the edge of the chromium contact (1-4 spots), which are negatively reflected in the current waveforms. The biggest interference was measured at point number 3. We believe that this is caused by the graphite leakage contact, which is located in this corner. So, to correctly interpret the measured results later, all measurements will be taken at point number 5, i.e. in the centre of the detector. We assume that the electric field inhomogeneities are minimal to negligible in the centre.

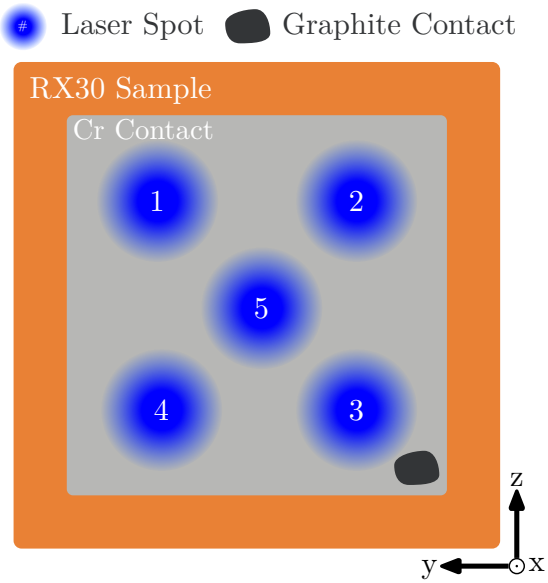

Figure 4.6: Positions (1-5) on RX30 detector for homogeneity measurement.

4.6 Measurement Repeatability

We use one setup for all measurements. So the primary question should be, are collected data comparable even though samples were alternated in apparatus? To test this premise we took one of our samples and measured three consecutive data with the same pulsing parameters. The first measurement was initial. Second, we took out and immediately returned the sample to the apparatus with a reset of the neutral density filter. And third, we re-calibrated the position of the laser beam on the sample. We obtained the same results within the noise for all three adjustments! Current waveforms are shown in figure 4.7. So we can achieve repeatable measurements.

4.7 Current-Voltage Characteristic

A current-voltage characteristic or I-V curve is a relationship between the electric current through a material and the corresponding voltage across it. Due to searching for voltage dependencies, we must take into consideration I-V characteristics. Mainly identify the type of potential hysteresis, so we could include them info experimental results and discussion. We operate from 0V to 150V. According to measurement we often move in this voltage interval up and down so knowing I-V dependencies is crucial for data explanation. For measuring I-V characteristics we use in-house-made apparatus. We measured I-V characteristics for all our samples from table 4.1. Voltage started from 0V to 150V and immediately continued back to 0V where rested for 1 hour. Then was applied same process but to negative voltages.

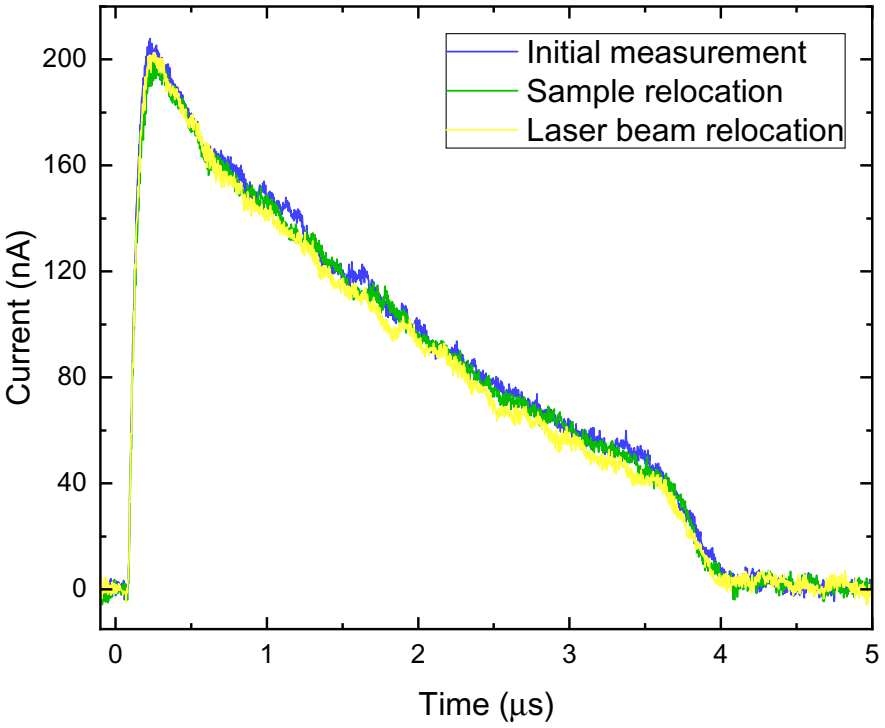

Figure 4.7: Raw data for measurement repeatability.

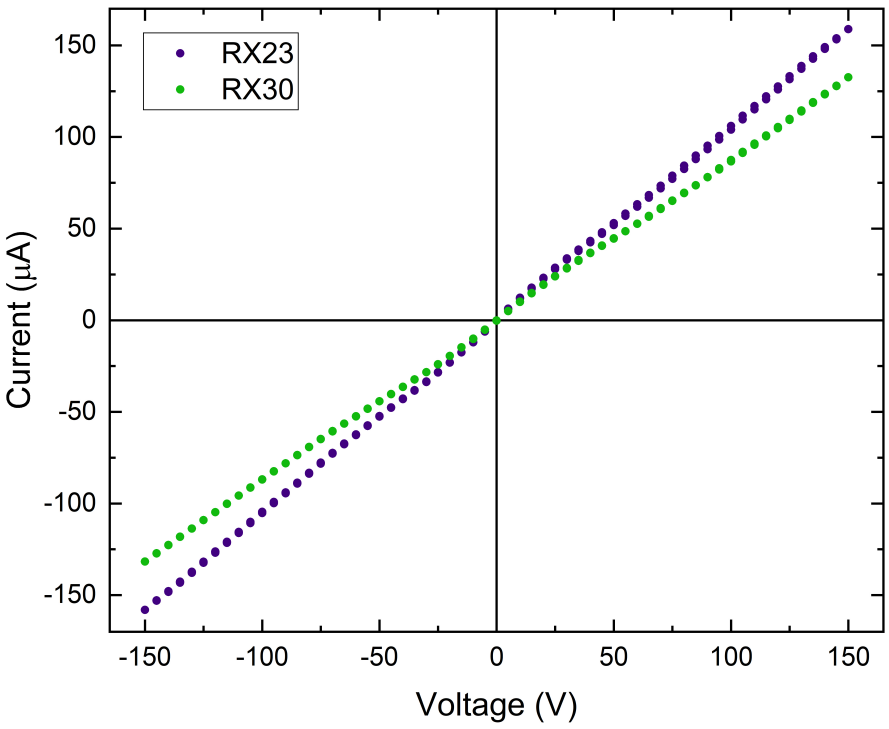

Figure 4.8: Current-voltage characteristic.

I-V dependencies are shown in figure 4.8. Luckily samples RX23 and RX30, supporting pillars of this work, mainly show linear behaviour in both voltage directions. It is obvious that sample RX23 is 1.2 times more conductive than RX30.

5. L-TCT Results and Discussion

This chapter summarizes and analyzes the measurements performed on the RX30 and RX23 samples presented in the previous chapter. We have used the methodology of transient currents induced by a laser diode of above-band-gap wavelength 450 nm according to the scheme shown in figure 4.3. After the light beam hits the surface of the detector, an electron-hole pair is generated under illuminated electrode. Due to applied bias electrons are immediately picked up by the anode contact and the holes, on the other hand, begin to drift towards the cathode. The drifting holes, according to the Shockley-Ramo theorem, induce a current, which we measure with an oscilloscope. The shape of measured current waveforms is mainly dependent on the pulsing parameters and the measurement history. By changing these variables our main goal is to describe the transport properties of $MAPbBr_3$ perovskites and to determine its basic transport properties such as drift mobility of charge carriers and their lifetimes.

The first step is to find the bipolar pulsing parameters (see scheme 4.1) with which the sample does not polarize during the measurement. In previous work [41] dealing with transport properties of the cadmium-zinc telluride, we used unipolar pulsing. Thus, the applied voltage to the sample reached only one polarity. This was only possible because of the absence of weakly bound ions in the CdZnTe material (we consider an ideal sample without mobile defects and impurities). The internal crystal structure and charge distribution remained identical - there was no polarization of the sample. However, the situation is different for $MAPbBr_3$ perovskites. When a unipolar voltage is applied to the sample, a slow drift of ions or impurities to the electrode of the appropriate polarity occurs. Physically moving ions can disrupt the perovskite structure and thus reduce the potential efficiency of the detector. To avoid this instability, we use bipolar voltage according to the scheme in figure 4.4. By pulsing both consecutive polarities in one period, we expect to return the deflected ion with the first polarity to its original position with the second polarity of the voltage pulse. However, though ion migration is one of the causes of degradation of perovskite devices, many of its aspects remain poorly understood [42].

5.1 First Attempt at Bipolar Pulsation

5.1.1 RX23

In the initial measurement, we wanted to confirm the basic thesis of bipolar pulsation. That is, whether unipolar pulsation is sufficient for measurements in the depolarized state. From the basic knowledge about perovskites obtained from the manufacturer, we chose the following pulsation parameters for the initial measurements $U+ = 100\,\mathrm{V}$, $U- = -100\,\mathrm{V}$, period $T = 100\,\mathrm{ms}$, bias pulse width $T+ = T- = 200\,\mu\mathrm{s}$ and laser pulse delay $100\,\mu\mathrm{s}$. The sample was under bias with these parameters for almost 9 hours and every 6 min we saved current waveform (cWF).

The time evolution of the hole current waveforms is shown in Fig. 5.1. The detector does not evolve during 8.5hours of measurement. The individual curves

go over each other and the transient time is the same. We have three possible models. First, during first $100\mu s$ of the period T a negative space charge forms in whole detector. Constant space charge creates linear electric field 3.26 defined with parameter a 3.17. From Monte Carlo simulation we get value of the parameter a, hole drift mobility and diffusion constant

$$\mu_h = 13.5\,\mathrm{cm}^2\,\mathrm{V}^{-1}\,\mathrm{s}^{-1} \text{ and } a = 15\,\mathrm{kV\,cm}^{-1} \text{ and } D = 0.7\,\mathrm{cm}^2\mathrm{V}^{-1}\mathrm{s}^{-1}.$$

We consider an infinite hole lifetime. Diffusion coefficient is twice as large as it should be according to the Einstein formula (2.4). The leading edge corresponds to the Gaussian bulk 3.30.

Second model, detector contains deep traps, so drifting hole have finite lifetime. From MC simulation trapping time and hole drift mobility is

$$\mu_h = 12\,\mathrm{cm}^2\,\mathrm{V}^{-1}\,\mathrm{s}^{-1} \text{ and } \tau_{TD} = 6\,\mu\mathrm{s} \text{ and } D = 0.7\,\mathrm{cm}^2\mathrm{V}^{-1}\mathrm{s}^{-1}.$$

In this model these pulsing parameters are sufficient to keep the RX23 detector in a state where no space charge is generated or space charge is generated but the depolarization time is sufficient to discharge it. This means that at the beginning of each period T the detector is in the same state. The depolarizing time ($T_{depol} = T - T_+ - T_-$) is long enough to depolarize the detector if needed. The ration of non-zero bias width to depolarization time is

$$\kappa = \frac{T_+ + T_-}{T_{\mathrm{depol}}} = \frac{T_+ + T_-}{T - (T_+ + T_-)} \doteq 0.4\%. \tag{5.1}$$

Comparing model with space charge and deep traps, space charge increases the transit time (3.27) which is offset by the increased mobility and so we got the same transit time for both simulations!

And third model, the contacts would not be concentric, or each contact would have a different dimension. We compared the contacts and saw no spatial differences. And that's why we're not developing this model further.

Furthermore, we wanted to confirm our assumption that in case of insufficient depolarization time the detector starts to evolve. So we took the same pulsing parameters and changed bias pulse width to $T+ = 500\,\mu\mathrm{s} = T-$. Bias was applied to the sample for over 1 hour and 20 minutes. We saved cWF every minute. The time evolution of the hole cWF is shown in Fig. 5.2. Dashed lines represent Monte Carlo simulation. Transit time is getting longer, so we choose a model with an space charge, which according to 3.27 prolongs the transit time. The electric field in the detector obtained from the Monte Carlo simulation is shown in the inset. The sample starts to develop from the initial state (purple colour curve) as we found out in Fig. 5.1. Main current plato decreases and transit time increases. Under contacts arises an electric field. This is due to the increasing space charge under the anode and cathode as well. The sample does not tend to return to its original state (purple curve) - the sample becomes polarized. Depolarization time ($T_{depol} = T - T_+ - T_-$) is not sufficient to depolarize the detector. A *memory effect* is created.[1]

[1] A measurement that is affected by the state of the previous measurement.

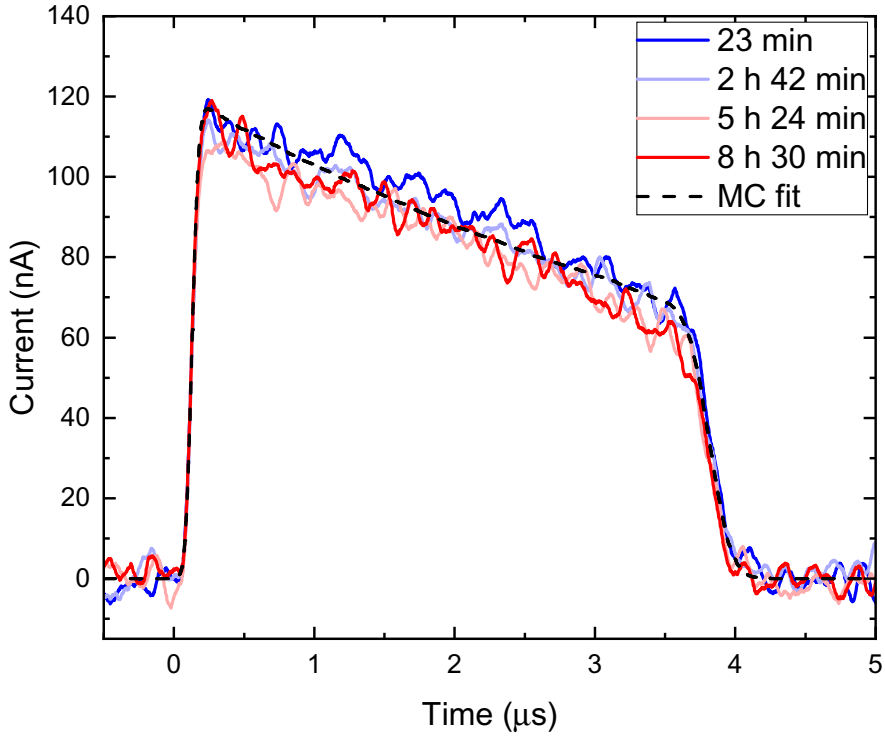

Figure 5.1: RX23 Sample. Time evolution of the hole current waveforms for pulsing parameters T = 100 ms, LPD = 100 μs, U+ = 100 V, U- = -100 V, T+,T- = 200 μs.

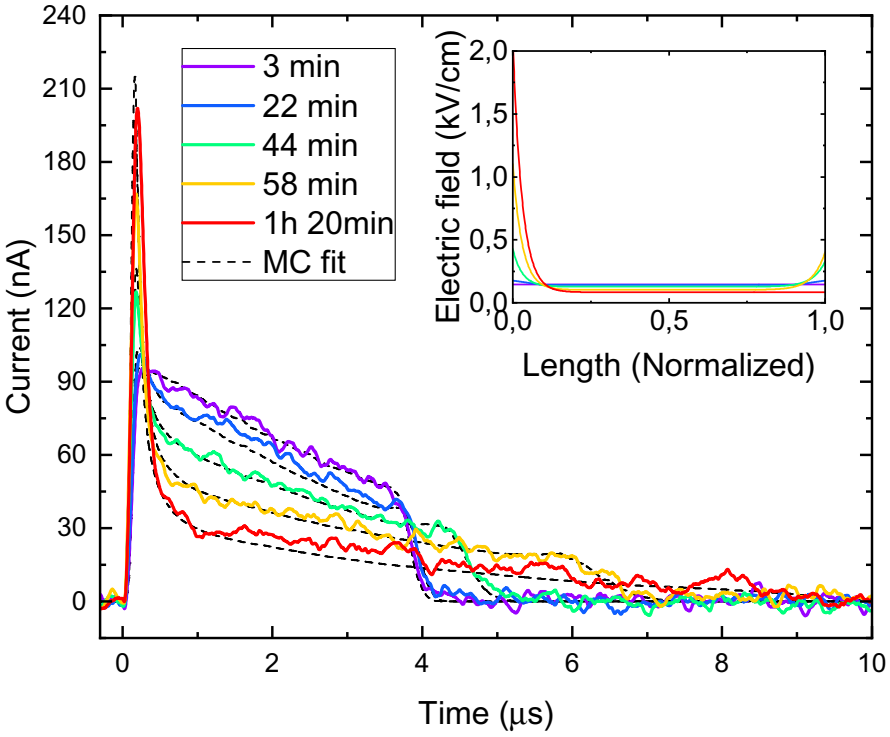

Figure 5.2: RX23 Sample. Time evolution of the hole current waveforms for pulsing parameters T = 100 ms, LPD = 100 μs, U+ = 100 V, U-= -100 V, T+,T- = 500 μs. **Inset:** Electric field obtained from MC simulation.

The slope of the central part of the cWFs slightly increases with time. We have same two models. First, the trapping time should increases with time or second, that the space charge along the length of the detector should decreases. The rising and falling edges begin to rise with time above the cWF level. This means that another space charge begins to build up under the anode and cathode. We used non-linear electric field in the Monte Carlo simulation shown in inset of figure 5.2 in form of two exponentials

$$E\left(x\right) = E_0 + ae^{-\frac{x}{LG}} + be^{\frac{x-L}{LM}}, \tag{5.2}$$

where M, G are new parameters indicating the exponential slope, and a, b are parameters of the magnitude of the electric field under anode and cathode. E_0 is calculated from bias (2.10), where we know bias. If we fix trapping time to $\tau_{TD} = 4.5\,\mu$s we get following parameters from MC simulation. Drift mobility decrease with time

$$\mu_h = 12.5\,\mathrm{cm^2V^{-1}s^{-1}} \;\rightarrow\; 8\,\mathrm{cm^2V^{-1}s^{-1}}. \tag{5.3}$$

For the last three measured times, exponential electric field under anode increase from

$$a = 3\,\mathrm{kVcm^{-1}} \;\rightarrow\; 10\,\mathrm{kVcm^{-1}} \;\rightarrow\; 20\,\mathrm{kVcm^{-1}}. \tag{5.4}$$

Electric field under cathode gained from MC simulation

$$b = 2\,\mathrm{kVcm^{-1}} \;\rightarrow\; 3\,\mathrm{kVcm^{-1}} \;\rightarrow\; 0\,\mathrm{kVcm^{-1}}. \tag{5.5}$$

The last zero value is due to small measured currents and large current error.

Within the measurement noise error, the cWF can be modeled with different electric field profiles. We took the current yellow curve for 58 minutes from the figure 5.2 and simulated it with a linear electric field and two different exponential electric fields, see figure 5.3. Despite the fact that we have different electric field profiles, we can see that all the cWFs are almost the same. They have the same transit time. And the leading and trailing edges have the same progress. The double magnitude of the exponential electric fields relative to the linear electric field at the edges is compensated by a smaller electric field in the sample volume to maintain the same bias (2.10). A spatial charge is needed here, otherwise the cWF would look like figure 5.4. The transit time would be significantly reduced and the overall shape of the current waveform would also be reduced. Exponential electric field can be easily approximated by linear electric field for which we already developed the theory in section 3.4.2.

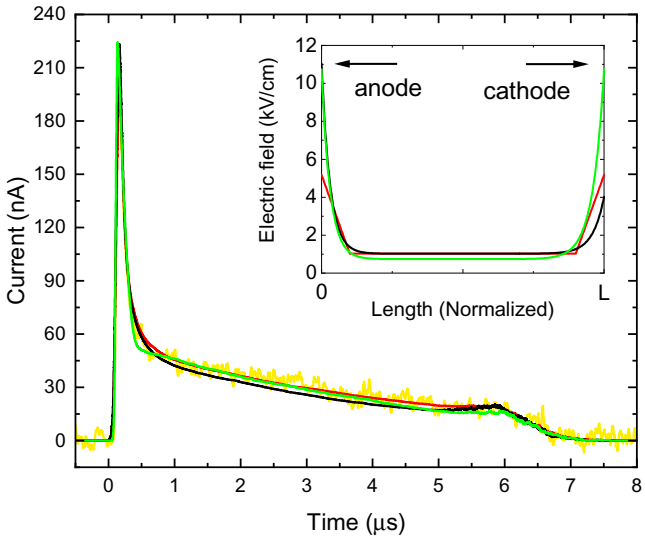

Figure 5.3: Monte Carlo simulation of yellow curve from figure 5.2 for different electric field profiles. Black is linear, red and green are exponential with different slope. This shows that different electric field shapes give the same cWF within our measurement error. All other parameters stay constant.

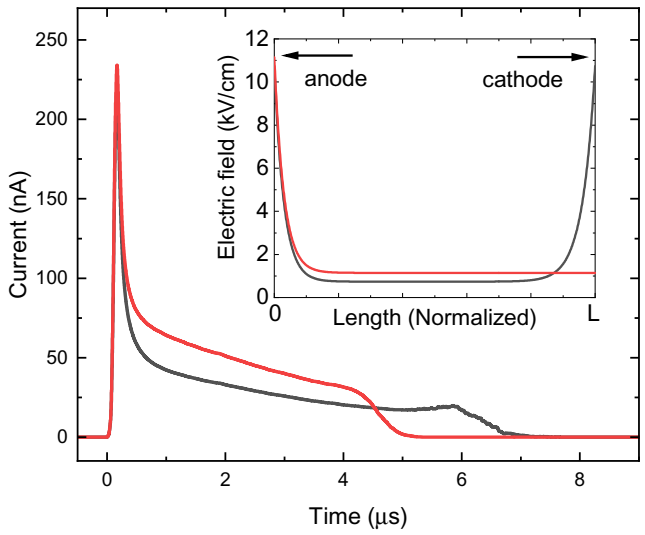

Figure 5.4: Monte Carlo simulation of yellow curve from figure 5.2 for different electric field profiles from the inset. Comparing situation with or without electric field under cathode. All other parameters stay constant.

5.1.2 RX30

Even if we have samples of the same material and manufacture, they have different measurement histories, so the relaxed state may be different. We selected the same pulsing parameters as for the RX23 sample, so bias $U+ = 100\,\mathrm{V}$, $U- = -100\,\mathrm{V}$, period $T = 100\,\mathrm{ms}$, bias pulse width $T+ = 200\,\mu\mathrm{s}$, $T- = 200\,\mu\mathrm{s}$ and laser pulse delay $LPD = 150\,\mu\mathrm{s}$ (we will continue to follow the labeling in this paper according to the scheme in figure 4.1) The sample was under bias with these parameters for 2.75 h and every 7.5 min we saved cWF. The resulting hole cWFs are shown in figure 5.5. cWFs resemble a rectangular profile for the

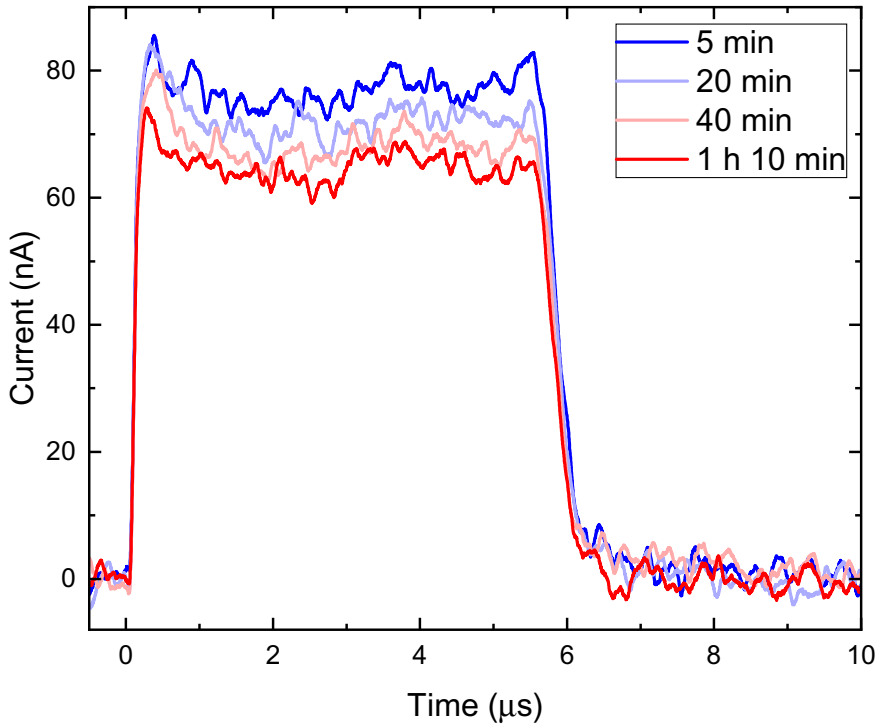

Figure 5.5: RX30 Sample. Time evolution of the hole current waveforms for fixed parametres LPD = 150 μs, U+ = 100 V, U- = -100 V, T+,T- = 200 μs, T = 100 ms.

entire measurement period. The maximum value of the leading and trailing edge currents are almost identical, thus the hole cloud drifts through the sample almost unchanged and the (3.6) formula can be used to determine the hole drift mobility

$$\mu_h = (13 \pm 3)\ \mathrm{cm^2V^{-1}s^{-1}}. \tag{5.6}$$

Transit time is determined by the time difference between the half of the maximum of the leading and the trailing edges. The average value of the current plateau between the edges of each cWF has a decreasing tendency. This is surface recombination - some of the photo-generated holes recombine before the drift begins (see chapter 3.7). The holes may recombine at the contact/sample interface or on defects from sample preparation. The precise mechanism of surface recombination has not yet been explained. If we consider traps, the lifetimes of the charge carriers are orders of magnitude larger than the measurement time. Thus, trapping levels cannot be detected at these pulsation parameters. We get a

combination of pulsation parameters for which the detector remains depolarized and does not evolve further, except for surface recombination, which will also stabilize.

We chose $LPD = 150\,\mu$s to see if the sample evolves during the first polarity $T+$. The rectangular cWF profile from this measurement can be described by theory from chapter 3.2 and thus no evolution occurs in this configuration. And therefore the current waveforms should be the same for $LPD = 100\,\mu$s. And indeed, when we change[2] the laser pulse delay to $LPD = 100\,\mu$s we get the same current waveforms as in the graph in figure 5.5, i.e. current cWFs with random noise between the leading and trailing edges that follows the rectangle. Transit time is the same - approx. $6\,\mu$s. The collected charge (time integral) of every cWF we measured is shown in figure 5.6, where the moving average is also marked. Time interval with surface recombination is visualized with arrows. The stabilization happens during the first 50 mins a since then, the sample is stable.

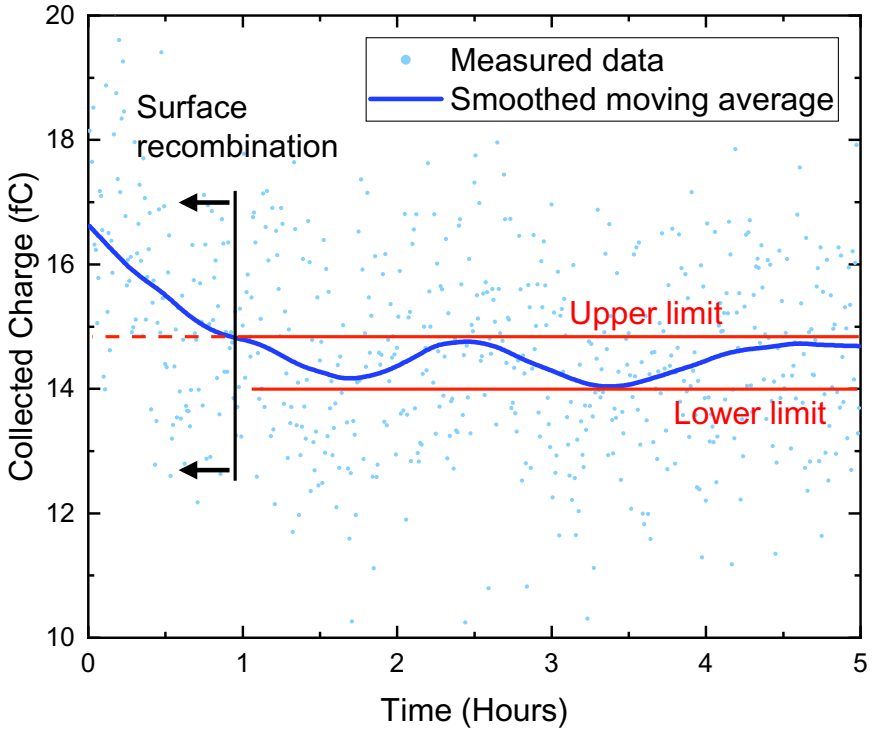

Figure 5.6: Sample RX30. Collected charge of the hole current waveforms. One blue dot represents one current WF. The blue line represents smoothed moving average. Parallel red lines represent the upper and lower limit of the blue line on time intervals starting at the first hour of the measurement. The black line and arrows indicate the time interval, where the surface recombination is noticeable.

[2]Because of the non-negligible RLC effects at $LPD < 80\mu$s, we choose mostly $LPD > 80\mu$s.

5.2 Bias Dependence

5.2.1 RX23 Sample

After finding the bipolar pulsation parameters preserving the detector in the depolarized state, we measured the bias dependence on the RX23 sample with the pulsing parameters $LPD = 100\,\mu s$, $T = 100\,\text{ms}$ and $T+ = 200\,\mu\text{s} = T-$. The bias dependence of the hole current waveforms of the R23 sample is shown in figure 5.7. Monte Carlo simulated waveforms are marked with a black dashed line. Bias normalized cWFs are shown in figure 5.8.

For the Monte Carlo simulation, there is again an ambiguity between the electric field inside the detector and the finite lifetime of the drifting charge. The current waveforms have a different slope. If we consider the space charge along the whole length of the detector, we would get an interval for the coefficient of the space charge (3.17)

$$a = -2.5\,\text{kV/cm} \;\rightarrow\; -9\,\text{kV/cm}. \tag{5.7}$$

So the magnitude of the space charge depends on the bias $a\,(U)$. On the other hand if we consider the finite lifetime, we get the trapping time

$$\tau_{TD} = 5.5\,\mu\text{s} \;\rightarrow\; 14\,\mu\text{s}. \tag{5.8}$$

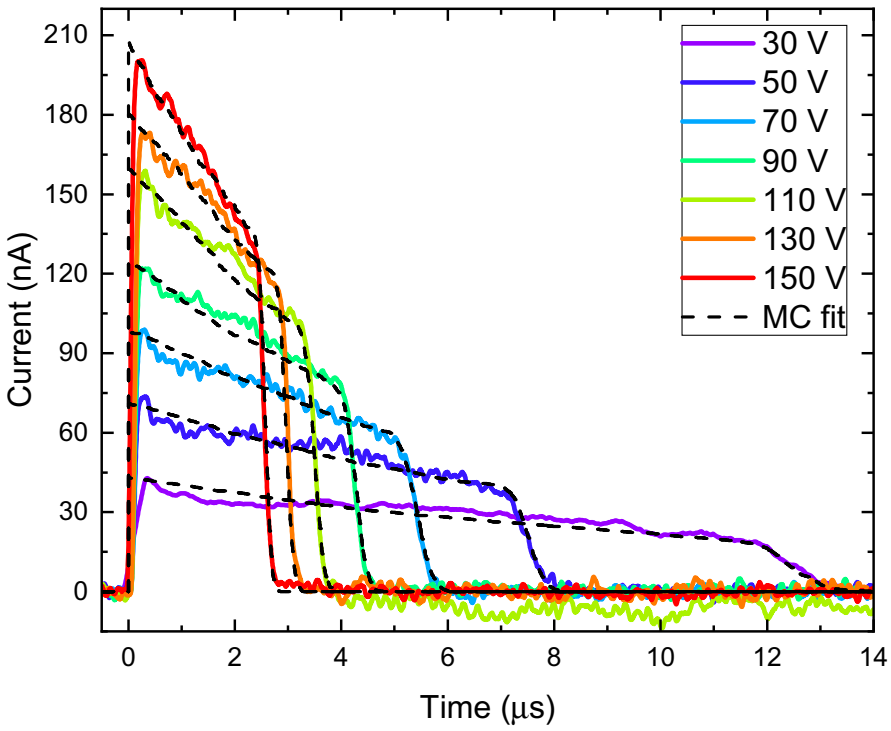

Figure 5.7: RX23 Sample. Pulsed bias dependence of the hole current waveforms with pulsing parameters LPD = 100 μs, T = 100 ms, T+,T- = 200μs. The black dashed line represent the Monte Carlo simulation.

For both Monte Carlo models we get the same hole mobility

$$\mu_h = (12 \pm 2)\ \mathrm{cm^2\,V^{-1}\,s^{-1}} \tag{5.9}$$

which is equivalent to the hole mobility of the RX30 sample. Diffusion constant for biases 70 V correspond with Einstein relation (2.4). For smaller biases is possible, that trapping time starts to combine with diffusion, because trailing edges get smaller quicker than says Einstein diffusion relation (2.4). The bias-normalized current waveforms from figure 5.7 are shown in figure 5.8. The bias-normalized hole waveforms start from the same point, therefore the same amount of the photo-generated charge will always begin to drift regardless of the bias difference, so surface recombination is not present.

After 3 μs they part ways. The slope is slightly different. If it were only life time, the curves would overlap, but they diverge slightly. Break occurs halfway through each cWF. This fact suggests that it is a spatial issue associated with the detector. The percentage loss of charge during drift is almost the same.

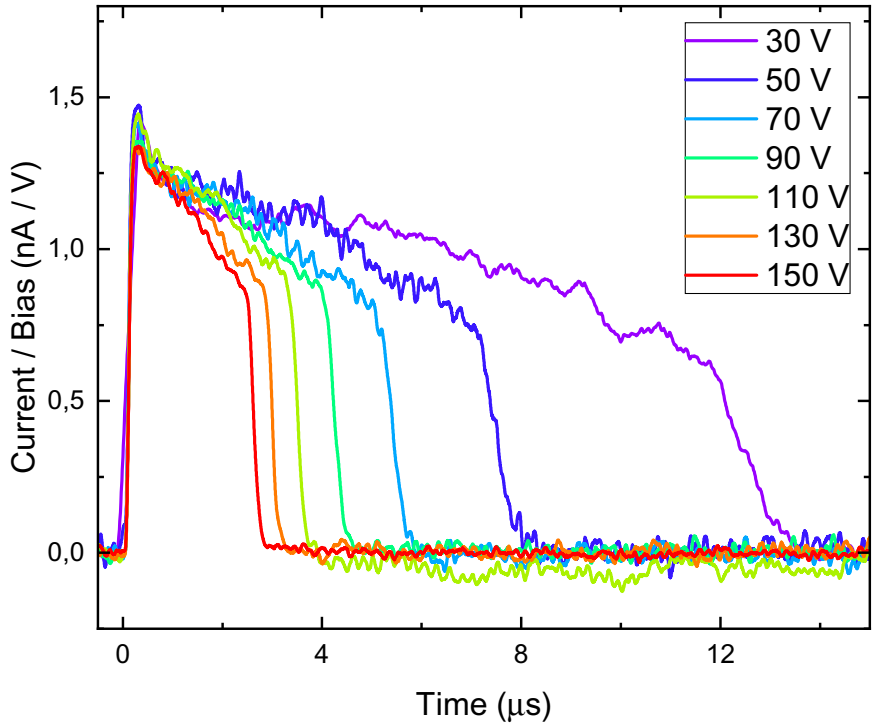

Figure 5.8: RX23 Sample. Bias-normalized pulsed bias dependence of the hole current waveforms from figure 5.7. The current of each cWf was divided by its bias.

5.2.2 RX30 Sample

After finding the bipolar pulsation parameters preserving the detector in the depolarized state, we measured the bias dependence with period $T = 100\,\text{ms}$, bias pulse width $T+ = 200\,\mu\text{s} = T-$ and laser pulse delay $LPD = 100\,\mu\text{s}$. Unfortunately, a fundamental mistake has been made. We accidentally applied DC bias to the sample instead of bipolar pulsed DC bias! Due to the lack of time, despite this error, we continued the measurement, but with the correct pulsation parameters. The more interesting result we got. So the bias dependence of hole current WFs is shown in figure 5.9. Black dashed lines represent the MC simulation. The electric field profiles obtained by MC simulation are shown in the inset of figure 5.9. One can notice from the left part of the sample an increasing area of the generally linear electric field. Where the part of the linear field is shortest for the largest bias 150 V. Otherwise, for the smallest bias, the linear electric field reaches a quarter of the sample. To maintain the bias on the electrodes according to formula (2.10), the residual electric field - the constant part, must decrease with the increasing part of the non-constant electric field, which the inset of the figure 5.9 confirms. This effect is reflected in the slope of the current WF following the leading edge. In parts of the constant electric field, the current WFs are constant. Thus, we estimate the lower limit of the lifetime of the holes to be $\tau_h \gg 60\,\mu\text{s}$ (from transit time of the 10V waveform). For voltages

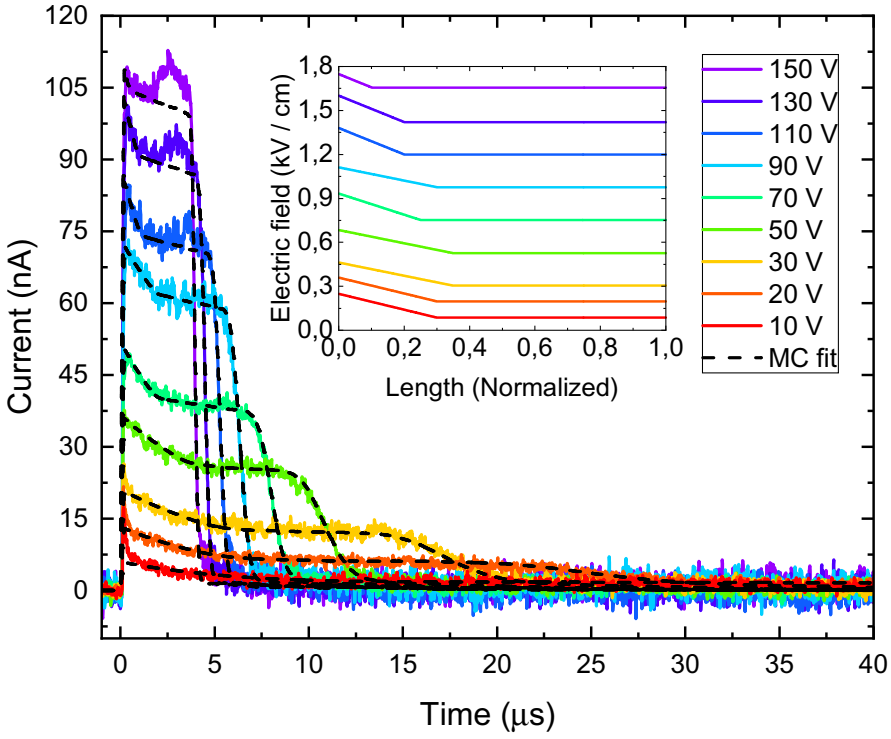

Figure 5.9: RX30 Sample. Pulsed bias dependence of the hole current waveforms with pulsing parameters LPD = 100 μs, T = 100 ms, T+,T- = 200μs. Black dashed lines represent the fit by Monte Carlo simulation. **Inset:** Electric field profile obtained by MC simulation.

higher than 90 V we see a sudden increase in the current before the falling edge. A space charge was created under the cathode due to a briefly applied DC voltage

and disappeared during the measurement. This is why we no longer see it for voltages of 90 V and smaller. We measured from 150 V to 10 V.

The bias-normalization of the hole current waveforms Fig. 5.9 are shown in Fig. 5.10. All current WFs after leading-edge start to decrease from the same value of normalized current. Thus, it is clear that surface recombination cannot be considered, because the same amount of holes starts drifting. But this is inconsistent with the measurement in the figure 5.5 where we measured surface recombination. It is possible that the gradual loss of current is hidden in a large measurement error. In MC simulation we defined one deep trap with the following parameters

$$\tau_{TD} = 5 \times 10^{-5}\,\mathrm{s}. \tag{5.10}$$

Einstein diffusion relation (2.4) is valid within the measurement error only for biases greater than 110V. For lower voltages, a layer may form under the contacts with a much lower lifetime than in the rest of the detector or a space charge may form. Below contacts could be a deep trap region that scales with bias. Both phenomena, or a combination of both, cause exponential drops at the beginning and end of the cWFs. We are unable to distinguish these phenomena from the measurements.

An interesting phenomenon is a fact that the sudden increase in current for higher voltages in the 5.9 figure, hereafter normalization, is not so noticeable. Measurement error - current fluctuations reach larger deflections than just the sudden current increase. Which is all due to the bias normalization.

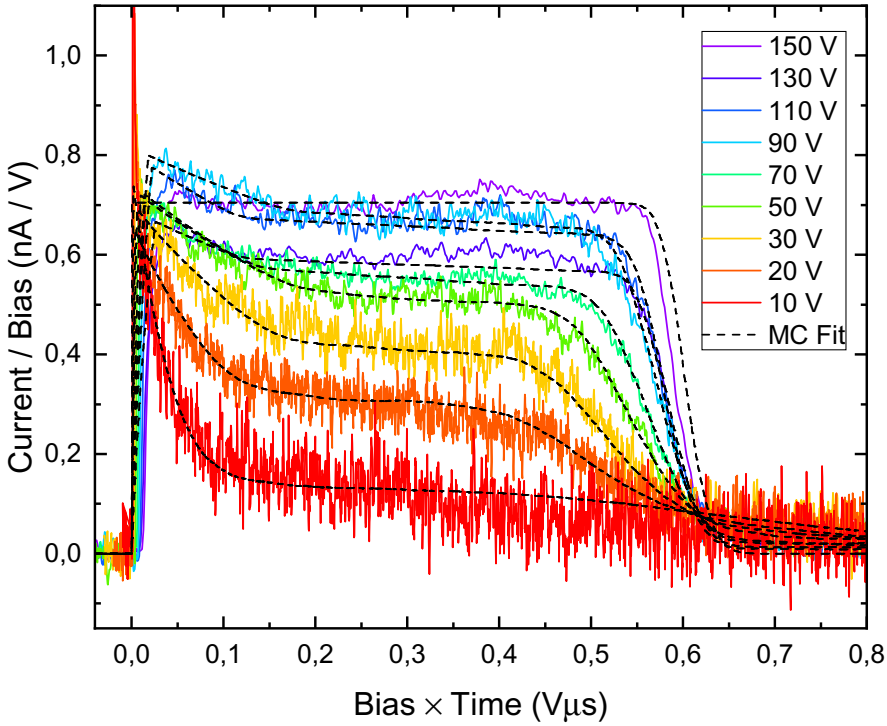

Figure 5.10: Bias-normalized pulsed bias dependence of the hole current waveforms in TSh geometry. LPD = 100 μs, T = 100 ms, T+,T- = 200μs. Black dashed lines represent the fit by MC simulation.

As a next parameter, we obtained the drift mobility of holes by fitting bias dependence of transit time, shown in Fig.5.11 by the equation (3.6)

$$\mu_h = (15 \pm 1)\ \mathrm{cm^2\,V^{-1}\,s^{-1}}. \tag{5.11}$$

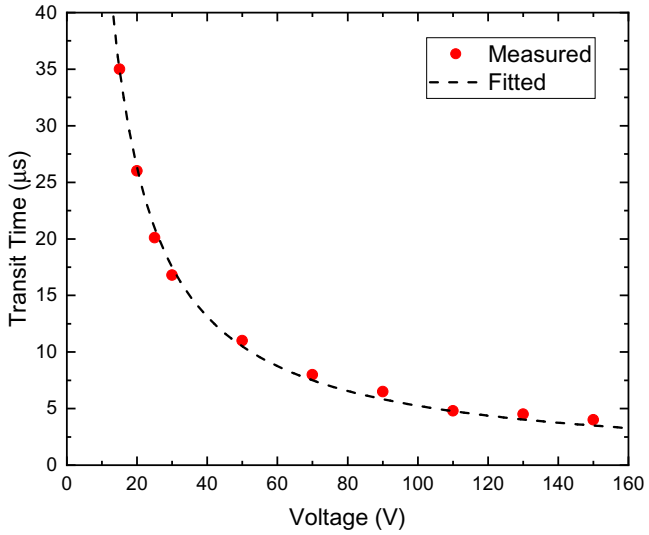

Figure 5.11: RX30 Sample. Transit time dependency of the hole current waveforms from figure 5.9. The black dashed line represents the theoretical model.

5.3 Bias Pulse Width Dependence

5.3.1 RX30 Sample

So the shape of the cWFs depends on whether the sample has enough time to depolarize. Thus, we further measured the bias pulse width dependence $T+, T-$ with fixed period T to determine the true effect of depolarization time ($T_{depol} = T - T_+ - T_-$). We stay with the period $T = 100\,\mathrm{ms}$ and voltage $U+ = 100\,\mathrm{V}$, $U- = -100\,\mathrm{V}$. Laser pulse delay is set to $LPD = 150\,\mu\mathrm{s}$ because we want to find out what happens at the end of the first polarity bias pulse. The bias pulse width dependence of the unpolarized detector is shown in Fig. 5.12. Monte Carlo cWFs simulations are marked with dashed lines. Electric field profiles from the Monte Carlo simulation are also included in the inset. Post-measurement relaxation is inserted in the figure 5.13.

We measured with $T+$, $T-$ from $150\,\mu\mathrm{s}$ to $600\,\mu\mathrm{s}$ each so whole nonzero bias pulse width was from $300\,\mu\mathrm{s}$ to $1.2\,\mathrm{ms}$. Polarization shows up at $T+ = 400\,\mu\mathrm{s} = T-$. Until then, $T+, T- < 400\,\mu\mathrm{s}$, cWFs curve behaves equally. The data are describable by the description in the section 3.2, i.e., the holes drift through the detector from the anode to the cathode without trapping in a homogeneous constant electric field. We can see the current drop from 80 nA to 60 nA for the two first cWFs so the surface recombination is again measurable. Relaxation after the last measurement on RX30 sample restored the surface recombination mechanism. The diffusion of the hole cloud is also present as we see a symmetrically stretched descending edge. But is five times bigger than should be according the Einstein relation (2.4).

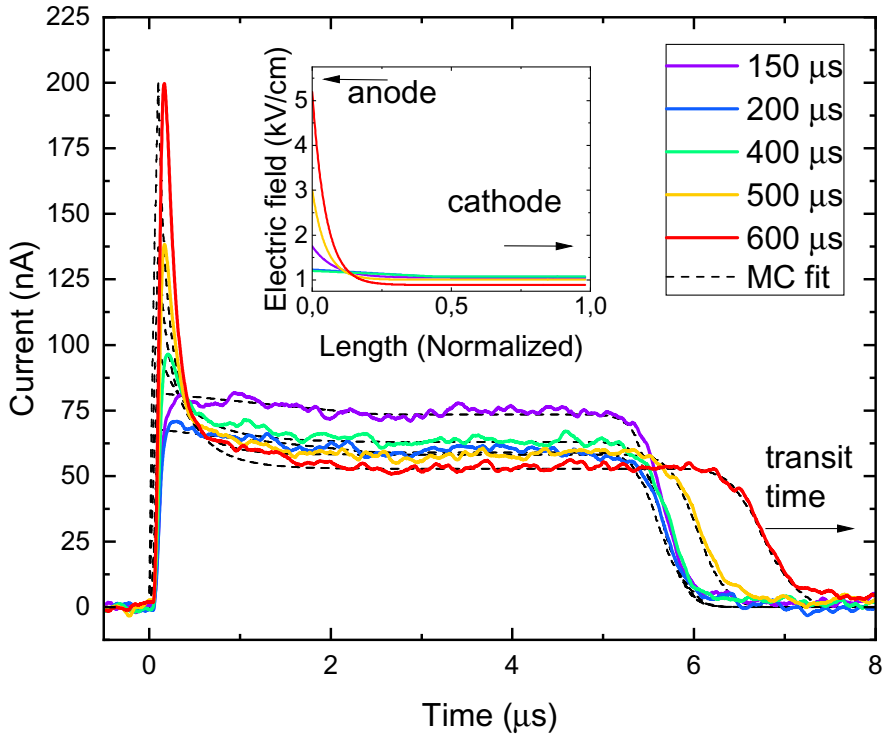

Figure 5.12: RX30 Sample. Bias pulse width dependence of the hole current waveforms with pulsing parameters LPD = 150 μs, U+ = 100 V, U- = -100 V, T+=T-, T = 100 ms. The transit time prolongation is marked with an arrow. Measured from 150 μs to 600 μs **Inset:** Electric field profile obtained by Monte Carlo simulation. The anode and cathode are also marked with arrows.

$T+ = T- \approx 350\,\mu$s is the maximum bias pulse width when polarization is not present. The ratio of non-zero bias pulse width to depolarization time is

$$\kappa = \frac{T_+ + T_-}{T_{\text{depol}}} = \frac{T_+ + T_-}{T - (T_+ + T_-)} \doteq 0.7\% \tag{5.12}$$

only! Polarization begins and from this point on, the space charge begins to accumulate under the anode. According to the Monte Carlo simulation, the space charge reaches up to a quarter of the sample. The next bias pulse width measurement is overshadowed by the already formed polarization and we talk about the so-called *memory effect*. This is why cWFs continue to evolve and transit time is increasing.

After measurement we set up pulsing parameters back to bias $U+ = 100\,$V, $U- = -100\,$V, period $T = 100\,$ms, bias pulse width $T+ = 200\,\mu s = T-$ and laser pulse delay to $LPD = 100\,\mu$s and once every 16 hours we measured few cWFs to know the current state. Relaxation cWFs are shown in the figure 5.13. We know from section 5.1 that these parameters don't polarize the detector during measuring a few cWFs. So if we can see some deviations from the rectangular shape, it means that the detector is polarized. And that is what we can see. The RX30 sample reached a depolarized state in 32 hours.

The evolution of the waveforms suggests that the region of the negative space charge forms under the anode. In the Monte Carlo simulation, we varied only the magnitude of the electric field. Transit time increases as the electric field

increases. Thus, there is no ambiguity between the electric field and the lifetime. The final lifetime of the carriers would not change the transit time.

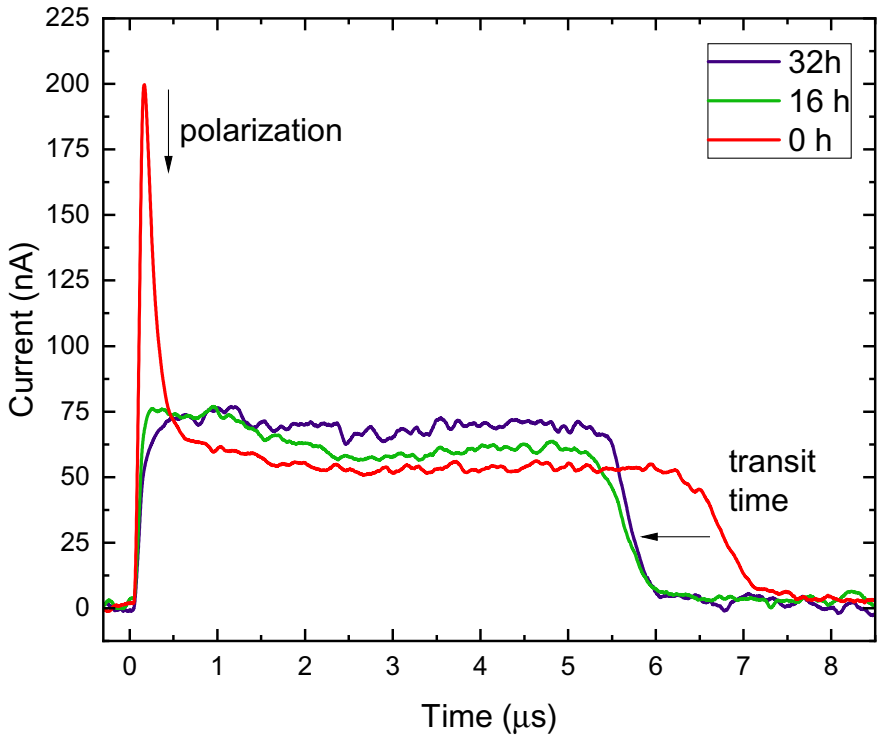

Figure 5.13: RX30 Sample. Relaxation within hours of a polarized detector. The red line is the red line in figure 5.12.

5.3.2 RX23 Sample

The situation for the RX23 sample is slightly different. Bias pulse width dependence for the RX23 sample is shown in figure 5.14. We measured with bias $U+ = 100\,\mathrm{V}$, $U- = -100\,\mathrm{V}$, laser pulse delay $LPD = 100\,\mu\mathrm{s}$ and period $T = 100\,\mathrm{ms}$. Monte Carlo simulations are marked with dashed lines. Electric field profiles from the Monte Carlo simulation are also included in the inset. Here, unlike the RX30, polarization also occurs underneath the cathode, which is evident by a hump on the trailing edge.

We measured with $T+, T-$ from $200\,\mu\mathrm{s}$ to $600\,\mu s$ each so whole nonzero bias pulse width was from $400\,\mu\mathrm{s}$ to $1.2\,\mathrm{ms}$. Polarization shows up at $T+ = 500\,\mu\mathrm{s} = T-$. Until then, $T+, T- < 500\,\mu\mathrm{s}$ cWFs curve behaves equally - linear decrease with the same slope between the leading and trailing edge. As we discussed in section 5.1.1, the slope can be realized by a deep traps or by a space charge in the sample. The first two cWFs (red lines) has the same slope but different size so again surface recombination is measurable. Diffusion of hole cloud is also present as we see a stretched trailing edge. The diffusion constant again does not fit Einstein's formula (2.4) by an order of magnitude.

$T+ = T- \approx 400\,\mu\mathrm{s}$ is the maximum bias pulse width when polarization is not present. The ration of non-zero bias pulse width to depolarization time is

$$\kappa = \frac{T_+ + T_-}{T_{\mathrm{depol}}} = \frac{T_+ + T_-}{T - (T_+ + T_-)} \doteq 0.8\% \tag{5.13}$$

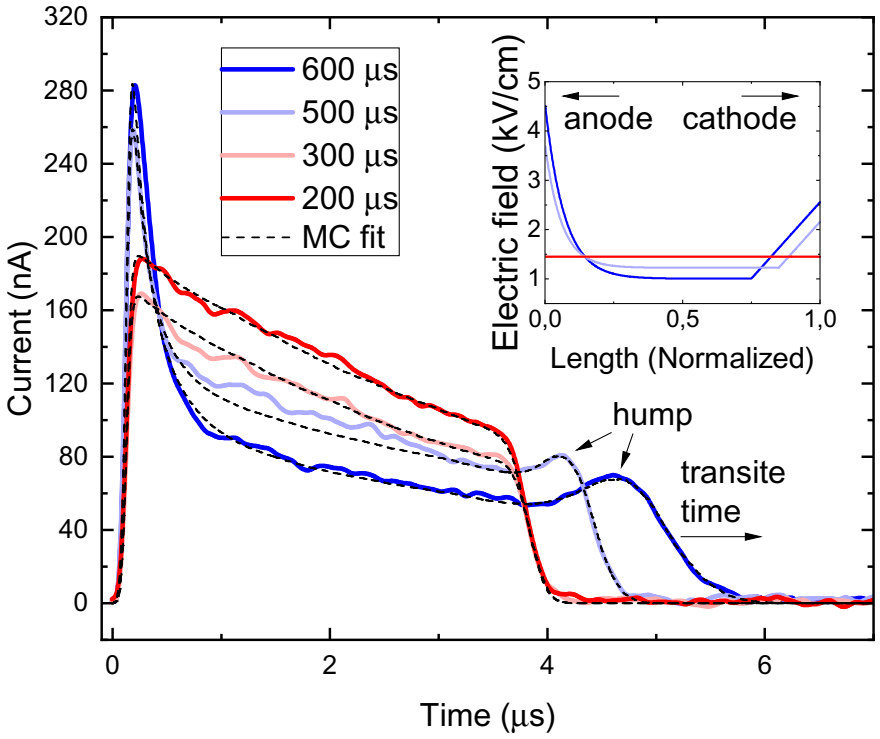

Figure 5.14: RX23 Sample. Bias pulse width dependence of the hole current waveforms with pulsing parameters LPD = 100 μs, $U+ = 100\,\mathrm{V}$, $U- = -100\,\mathrm{V}$, $T+ = T-$, $T = 100\,\mathrm{ms}$. The transit time prolongation is marked with an arrow. Measured from $200\,\mu s$ to $600\,\mu$s. **Inset:** Electric field profile obtained by Monte Carlo simulation. The anode and cathode are also marked with arrows.

only! Polarization begins and from this point on, the space charge begins to accumulate under the anode and cathode as well. According to the Mote Carlo simulation the space charge is distributed in the first and last quarter of the sample. Memory effect is also present. so measurement for $T+ = T- > 300\,\mu$s is biased by the measurement history for $T+ = T- < 300\,\mu$s.

5.4 T- Bias Pulse Width Dependence RX30

The next parameter we were changing was the width of the second bias pulse $T-$. This is a parameter which we discussed at the beginning of this chapter. After a few days of relaxation, we prepared the measurement and during configuration, we accidentally applied DC bias to the sample for about 5 seconds. To find out what state the sample is in, we measured one cWF at the depolarizing parameters from the first section of this chapter ($T = 100\,\mathrm{ms}$, $T+, T- = 200\,\mu\mathrm{s}, U+ = 100\,\mathrm{V}, U- = -100\,\mathrm{V}$ and $LPD = 100\,\mu$s). We got the same waveform as the red curve in the graph in figure 5.12. So the sample became polarized immediately! So we let the sample relax for a week. After one week, we again measured the current state of the sample with depolarizing pulsation parameters. Even after a week of relaxation, we did not get an ideal rectangular cWF, cWF had a section of linear current drop at the beginning which we consider a new steady state! It is possible that if we let the sample relax for a few weeks, the sample

would thermally return to the fully depolarized state where we would again get ideal rectangular waveforms, but this is not within the time capabilities of our measurements. Therefore, we continued the measurements anyway.

We started measuring with pulsing parameters that do not polarize the sample, bias $U+ = 100\,\mathrm{V}$, $U- = -100\,\mathrm{V}$, period $T = 100\,\mathrm{ms}$, bias pulse width $T+ = 200\,\mu\mathrm{s} = T-$ and laser pulse delay $LPD = 150\,\mu\mathrm{s}$ and we lowered the bias pulse width $T-$ from $200\,\mu s$ to $0\,\mu s$. As before we set the laser pulse delay to $150\,\mu\mathrm{s}$ because it tells us the behaviour at the end of the first bias pulse. Bias pulse width $T-$ dependence of the hole current waveforms is shown in Fig. 5.15. Monte Carlo simulated cWFs are marked with dashed lines. The inset shows an electric field simulated by the MC method. The blur effect of the amplifier resembling a shallow trap is also marked with the arrow.

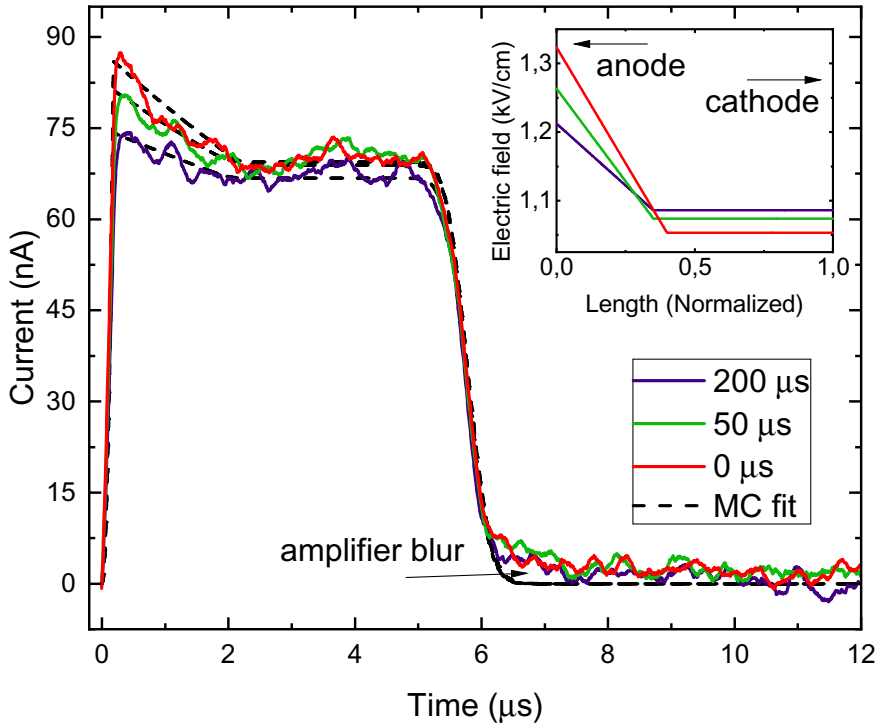

Figure 5.15: RX30 Sample. Bias pulse width $T-$ dependence of the hole current waveforms with pulsing parameters T = 100 ms, T+ = 200 μs, U+ = 100 V, U- = -100 V, LPD = 150 μs. Monte Carlo simulated cWFs are marked with dashed lines. **Inset:** Electric field profile obtained by Monte Carlo simulation. The anode and cathode are also marked with arrows.

For $T- = 200\,\mu\mathrm{s}$ we obtain a hint of a rectangle which is our new stable state (see Fig. 5.5 for the previous stable state). We started from this curve. So if we decrease bias pulse width $T-$, the initial leading edge starts to increase. Depolarization time becomes insufficient for the total depolarization of the detector. A negatively charged space charge begins to form under the anode so the beginning of the cWFs begins to tilt negatively. And as we continue to measure the polarization it adds up and the *memory effect* is present. Transit time is not shifted yet, because the polarization does not reach such values as in the measurement in section 5.3 (see figure 5.12 for comparison).

We repeated the measurement with the period $T = 2\,s$ to determine the effect

of the depolarization time. Now depolarization time is more than 20 times longer than before. The situation is the same as in figure 5.15. The first almost half of the detector is starting to polarize. The evolution of the waveforms suggests that the region of the negative space charge forms under the anode. The other half of the detector remains in its original state. Thus, we can say that in the time-resolved capabilities of our apparatus, we are not able to use the period length to achieve a sufficiently long depolarization time for those pulsing parameters. This measurement again proves the effectiveness of bipolar pulsing!

5.5 Depolarization Time Dependence RX30

In the first section of this chapter, we found pulsation parameters at which the current waveform showed no time evolution. Thus, even if the detector becomes polarized during a bias pulse, the time at which is no bias applied is sufficient for eventual depolarization. During the depolarization time, the sample should depolarize. The accumulated space charge should back move to the most energetically favourable positions and thus the detector should go into a state, as was before measurement.

We chose a symmetric bias pulse long enough to polarize our sample, so $T+ = T- = 500\,\mu s$. On the other hand, the longer depolarization time we have to choose to start the measurement from the unpolarized state. Depolarization time dependence of the hole current waveforms for $T+ = T- = 500\,\mu s$ is shown in figure 5.16. Monte Carlo simulations are marked by dashed lines and the electric field is shown in the inset.

Polarization starts to become more apparent around period $T = 400\,ms$ for bias width $T+ = T- = 500\,\mu s$. Negative space charge starts to accumulate under the anode. The ratio of non-zero bias pulse width to depolarization time is

$$\kappa = \frac{T_+ + T_-}{T - (T_+ + T_-)} \doteq 0.3\% \tag{5.14}$$

only! Since the first polarization starts to appear, the next measurement is affected by the *memory effect*. Transit time starts to prolong with the last measured cWF. It is due to the arising field under the anode caused by the arising space charge. As a reminder, if it were the lifetime of the carriers - the presence of deep traps - the transit time would not change. So we hole lifetime is infinity.

From Monte Carlo simulation we get hole drift mobility and diffusion coefficient

$$\mu_h = 14.5\,\mathrm{cm^2\,V^{-1}\,s^{-1}} \text{ and } D = 1.7\,\mathrm{cm^2 V^{-1} s^{-1}},$$

where electric field was simulated by exponentials (5.2). The lifetime of the holes is much bigger than the time resolution of the measurements.

From all the measurements made so far, perovskites $MAPbBr_3$ appear to be rather unstable detectors concerning the parameters. It is therefore important to note that a relaxed state developed due to the short application of DC voltage. And that is exactly what is beginning to manifest itself here. The full red curve in the picture 5.16 for $T = 800\,\mu s$ is the relaxed state for RX30 and we can see a hint of the polarization at the beginning of the graph. We have not been able to get rid of this artefact. This fact is attributed to the change in the internal structure

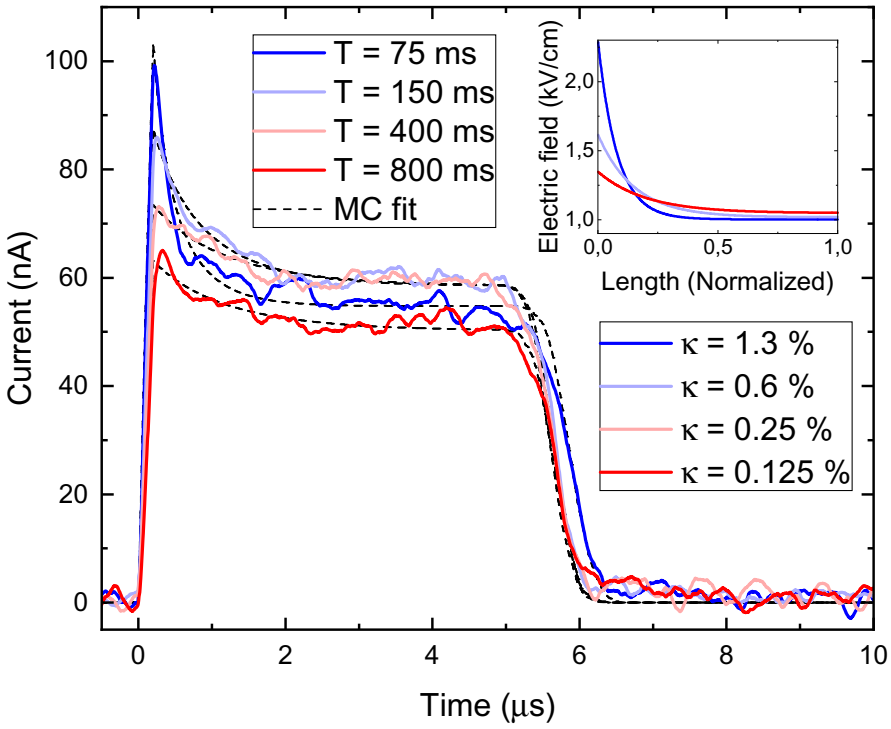

Figure 5.16: RX30 Sample. Depolarization time dependence of the hole current waveforms with pulsing parameters LPD = 150 μs, U = 100 V, T+,T- = 500 μs. Black dotted lines represent MC simulation. **Inset:** Electric field profile obtained by MC simulation.

of the detector when a DC bias is applied. By comparing the electric field in the inset plots in figure 5.12 and 5.15 (before and after the DC bias is applied), it is clear that the space charge forms almost to the middle of the detector instead of a quarter of the detector.

5.6 Laser Pulse Delay Dependence

Up to this point, we have varied the pulsing parameters that specify the shape of the bias pulsing (see schematic in figure 4.1). But now we will keep the pulsing parameters constant and change only the laser pulse delay LPD. This will give us knowledge of how the sample evolves during the bias pulse. Again we set the pulsing parameters to $T+ = 200\,\mu s = T-$, period $T = 100\,ms$, bias $U+ = 100\,V$, $U- = -100\,V$. We know from previous measurements that these pulsation parameters do not create a memory effect. Laser pulse delay dependence of the hole current waveforms is shown in Fig. 5.17.

We can see that at the end of the bias pulse the detector starts to polarize - a small bump starts to grow at the beginning of the waveforms. The current within the measurement error starts to decrease from the value 180 nA and descends in a straight line which means there's a space charge or deep trap inside the detector, as discussed in the first section of this chapter. This behaviour can be explained by the gradual expansion of the deep trap region under the anode (e.g. impurities) into the sample. So at the beginning of the drift, we have the same number of holes that start drifting through the detector towards the cathode. At

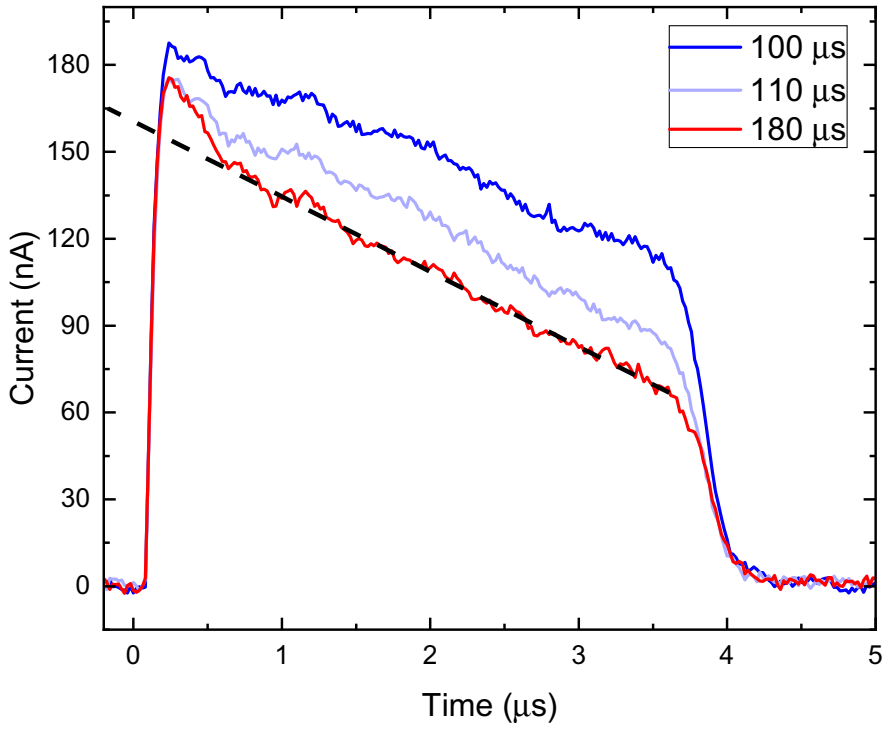

Figure 5.17: RX23 Sample. Laser pulse delay dependence of the hole current waveforms with pulsing parameters T = 100 ms, T+,T- = 200 μs, U+ = 100 V and U- = -100 V.

the beginning of the detector, they pass through a deep trap region where some of the charges are absorbed. If the region of traps begins to stretch, more charge will be captured. When the drifting charge leaves the trap region it begins to behave as in the previous cases without the extended trap area. As discussed in section 5.1.1.

5.7 Electron Bias Dependence

Up to now, we have been concentrating on the majority carriers, namely the holes. So electrons are minority charge carriers. Pulsed bias dependence of the electron current waveforms is shown in figure 5.18. We use the following pulsing parameters. Period $T = 100\,\mathrm{ms}$, laser pulse delay $LPD = 100\,\mu\mathrm{s}$ and bias pulse width $T+ = 200\,\mu\mathrm{s} = T-$. In this measurement, we had to set the maximum intensity of the light beam to detect anything at all. We were not able to find the pulsating parameters to obtain the transit time. Electrons are subject to strong trapping on the traps. This is why we see exponential drops for all biases.

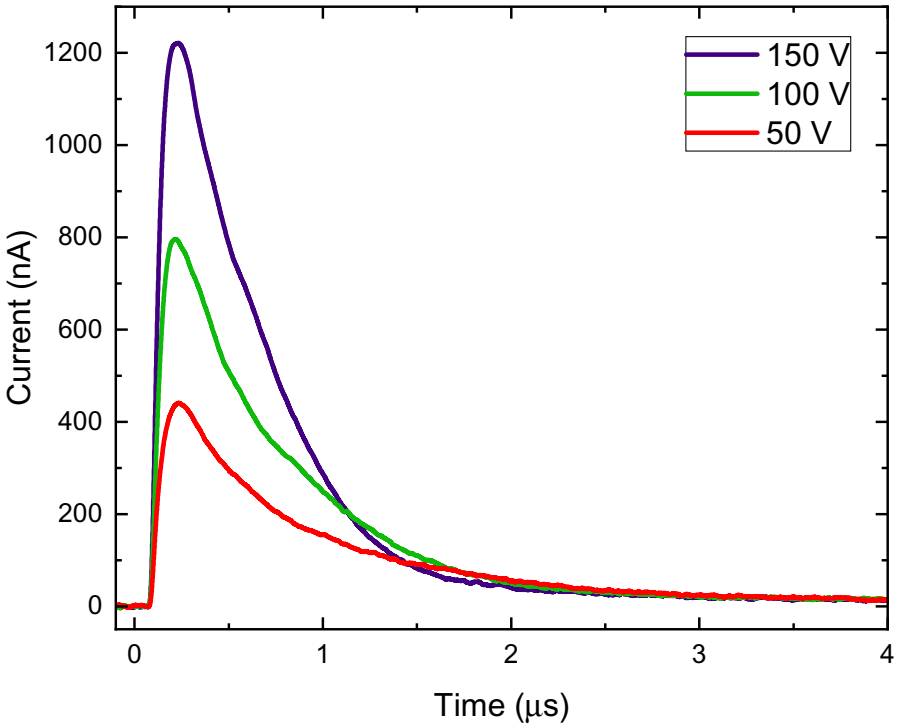

Figure 5.18: RX23 Sample. Pulsed bias dependence of the electron current waveforms with pulsation parameters T = 100 ms, LPD = 100 μs and T+,T- = 200 μs. The used bias in the legend is the absolute value of biases U+ and U-. First polarity was positive and the second polarity was negative.

Conclusion

This thesis presents a description of the charge transport in methylammonium lead tribromide perovskites $CH_3NH_3PbBr_3$ using bipolar bias pulsed Laser - induced Transient Current Technique and in-house made Monte Carlo simulation software for simulating the measured current waveforms. In the first chapter *Introduction* we have explained the basic problem that perovskites face today such as degradation due to moisture, temperature and general traps inside the material. In the next theoretical section *Kinematics of Charge Carriers in Detector*, we defined the necessary equations such as the drift-diffusion equation and the continuity equation, which are used to derive the theoretical current waveforms in other parts of the paper. We have also defined a detector model on which we simulate the current waveforms throughout the paper. The following also theoretical chapter *Charge Distribution and Current Response* finally contains individual examples of possible current waveforms, including the basic charge density drift in the form of a delta function, we have also included charge lifetimes formed by the shallow and deep trap. We have derived the possibility that the entire detector contains space charge and its effect on the overall electric field inside the detector. We have discussed possible charge densities and their effect on the leading edge of current waveforms. And in the last theoretical part, we described a possible theoretical model of surface recombination. All these models contain a graphical interpretation of the theoretically calculated current waveform, which allows us to identify individual phenomena in real current waveforms.

Experiment chapter contains a description of the measuring apparatus and a description of the measured samples, which were obtained from the *Université Grenoble Alpes* and *Cea-Leti*. We also justified the choice of the spot on the detector on which we shine and confirmed that our apparatus allows repeatable measurements despite the fact that we change samples during the measurement.

The last chapter *L-TCT Results and Discussion* contains all pulsed L-TCT results measured on two methylammonium lead tribromide perovskite samples. Almost all measured waveforms include Monte Carlo simulation based on the arbitrary electric field, two trap levels, diffusion effects and laser pulse shape. First, we searched for the pulsation parameters of the applied bias to obtain a basic measurement configuration in which the detector does not polarize and no memory effect occurs. In this step, we confirmed the basic assumption of the advantage of bipolar pulsation instead of unipolar pulsation. Using only one polarity in a single pulse, both samples became polarized and it was necessary to wait several hours to days for the sample to depolarize spontaneously. On the other hand, when using both polarities in one pulse-bipolar pulsing the detector was stable, it did not polarize for hours (we did not measure longer periods). This was followed by sections in which we examined the effect of individual pulsing parameters such as the bias pulse width, second polarity pulse width, depolarization time, laser pulse delay and bias. Almost each section contained two subsections dealing with each sample separately and their comparison with each other when changing the same parameter. Whichever parameter we varied, we always got the same pattern of behaviour of the perovskites we studied.

We get a depolarized detector if we pulse a symmetrical bipolar bias pulse

with a sufficiently long depolarization time. We have obtained a ratio of the time length of the applied bias to the depolarization time of about 0.3% only! If a shorter depolarization time or longer bias pulse width is used perovskite starts to polarize immediately and the memory effect starts to grow. The first positive voltage will slightly depolarize the detector. The following negative bias, rather than depolarizing effects, serves here to keep it in its current state. It is not clear from the measurements that the negative bias helps in depolarization. After the bias is set to zero, the sample started to depolarize. The length of the depolarization time determines whether the sample can completely depolarize or not. In the case of asymmetric pulsation at the same bias pulse width but the different magnitude of biases the sample immediately begins to polarize. Our apparatus is capable of setting a two-second depolarization time, but even this was insufficient for depolarization.

The RX30 sample is polarized under the anode, while RX23 is polarized under the cathode as well. We measured the drift mobility of the holes around $13\,\mathrm{cm^2V^{-1}s^{-1}}$. The hole cloud is subject to diffusion. The polarization described above can be explained by two phenomena. The first explanation, below the contacts, is the trapping section which thanks to bias gradually expands into the sample, causing the current drop we see in the waveforms. Whether this is impurities or drift of the perovskite ions themselves we are unable to determine. And the second consecration is in motion of space charge creating a non-constant electric field again causing the current to drop. Or it's a combination of both.

This is a unique approach to bipolar voltage measurement that is just beginning to appear in other scientific papers. Results similar to these were not found at the time of writing.

The perovskites we have studied are very sensitive to the measurement conditions, but still show signs of a prospective detector. We created several models and descriptions of the internal transport, but none were reliable. It is therefore interesting to continue the research and to fully describe the charge carrier transport mechanism inside the detector. As a follow-up measurement, it would be interesting to test asymmetric bipolar pulsing, where the time integral of the voltage of each polarity is preserved. In a future study, the temperature dependence of the current waveforms should be used to evaluate all parameters of traps, e.g. trap energy, capture cross section or trap concentrations to push the knowledge of perovskites a little further. Looking beyond photovoltaics, MHPs continue to demonstrate the huge potential for application in a wider range of optoelectronics including lasers, electromagnetic photodetectors, and light-emitting diodes to name a few.

Bibliography

[1] Anton R. Chakhmouradian and Patrick M. Woodward. Celebrating 175 years of perovskite research: a tribute to roger h. mitchell. Physics and Chemistry of Minerals, 41(6):387–391, May 2014.

[2] Quinten A. Akkerman, Gabriele Rainò, Maksym V. Kovalenko, and Liberato Manna. Genesis, challenges and opportunities for colloidal lead halide perovskite nanocrystals. Nature Materials, 17(5):394–405, February 2018.

[3] Roger H. Mitchell, Mark D. Welch, and Anton R. Chakhmouradian. Nomenclature of the perovskite supergroup: A hierarchical system of classification based on crystal structure and composition. Mineralogical Magazine, 81(3):411–461, June 2017.

[4] Kei Hirose, Ryosuke Sinmyo, and John Hernlund. Perovskite in earth's deep interior. Science, 358(6364):734–738, November 2017.

[5] T. He, Q. Huang, A. P. Ramirez, Y. Wang, K. A. Regan, N. Rogado, M. A. Hayward, M. K. Haas, J. S. Slusky, K. Inumara, H. W. Zandbergen, N. P. Ong, and R. J. Cava. Superconductivity in the non-oxide perovskite MgCNi3. Nature, 411(6833):54–56, May 2001.

[6] Wei Li, Zheming Wang, Felix Deschler, Song Gao, Richard H. Friend, and Anthony K. Cheetham. Chemically diverse and multifunctional hybrid organic–inorganic perovskites. Nature Reviews Materials, 2(3), February 2017.

[7] Heng-Yun Ye, Yuan-Yuan Tang, Peng-Fei Li, Wei-Qiang Liao, Ji-Xing Gao, Xiu-Ni Hua, Hu Cai, Ping-Ping Shi, Yu-Meng You, and Ren-Gen Xiong. Metal-free three-dimensional perovskite ferroelectrics. Science, 361(6398):151–155, July 2018.

[8] Sergey N. Britvin, Sergei A. Kashtanov, Maria G. Krzhizhanovskaya, Andrey A. Gurinov, Oleg V. Glumov, Stanislav Strekopytov, Yury L. Kretser, Anatoly N. Zaitsev, Nikita V. Chukanov, and Sergey V. Krivovichev. Perovskites with the framework-forming xenon. Angewandte Chemie, 127(48):14548–14552, October 2015.

[9] Juan-Pablo Correa-Baena, Michael Saliba, Tonio Buonassisi, Michael Grätzel, Antonio Abate, Wolfgang Tress, and Anders Hagfeldt. Promises and challenges of perovskite solar cells. Science, 358(6364):739–744, November 2017.

[10] Kebin Lin, Jun Xing, Li Na Quan, F. Pelayo García de Arquer, Xiwen Gong, Jianxun Lu, Liqiang Xie, Weijie Zhao, Di Zhang, Chuanzhong Yan, Wenqiang Li, Xinyi Liu, Yan Lu, Jeffrey Kirman, Edward H. Sargent, Qihua Xiong, and Zhanhua Wei. Perovskite light-emitting diodes with external quantum efficiency exceeding 20 per cent. Nature, 562(7726):245–248, October 2018.

[11] Quinten A. Akkerman and Liberato Manna. What defines a halide perovskite? ACS Energy Letters, 5(2):604–610, January 2020.

[12] Best research-cell efficiency chart.

[13] Constantinos C. Stoumpos, Christos D. Malliakas, and Mercouri G. Kanatzidis. Semiconducting tin and lead iodide perovskites with organic cations: Phase transitions, high mobilities, and near-infrared photoluminescent properties. Inorganic Chemistry, 52(15):9019–9038, July 2013.

[14] George Kakavelakis, Murali Gedda, Apostolis Panagiotopoulos, Emmanuel Kymakis, Thomas D. Anthopoulos, and Konstantinos Petridis. Metal halide perovskites for high-energy radiation detection. Advanced Science, 7(22):2002098, October 2020.

[15] Qi Wang, Yuchuan Shao, Haipeng Xie, Lu Lyu, Xiaoliang Liu, Yongli Gao, and Jinsong Huang. Qualifying composition dependent p and n self-doping in CH3NH3PbI3. Applied Physics Letters, 105(16):163508, October 2014.

[16] Yukari Takahashi, Hiroyuki Hasegawa, Yukihiro Takahashi, and Tamotsu Inabe. Hall mobility in tin iodide perovskite CH3nh3sni3: Evidence for a doped semiconductor. Journal of Solid State Chemistry, 205:39–43, September 2013.

[17] Haotong Wei and Jinsong Huang. Halide lead perovskites for ionizing radiation detection. Nature Communications, 10(1), March 2019.

[18] Alan Owens and A. Peacock. Compound semiconductor radiation detectors. Nuclear Instruments and Methods in Physics Research Section A: Accelerators, Spectrometers, Detectors and Associated Equipment, 531(1-2):18–37, September 2004.

[19] Pronoy Nandi, Chandan Giri, Diptikanta Swain, U. Manju, and Dinesh Topwal. Room temperature growth of CH3NH3PbCl3 single crystals by solvent evaporation method. CrystEngComm, 21(4):656–661, 2019.

[20] Tao Ye, Xizu Wang, Xianqiang Li, Alex Qingyu Yan, Seeram Ramakrishna, and Jianwei Xu. Ultra-high seebeck coefficient and low thermal conductivity of a centimeter-sized perovskite single crystal acquired by a modified fast growth method. Journal of Materials Chemistry C, 5(5):1255–1260, 2017.

[21] Fang Yao, Jiali Peng, Ruiming Li, Wenjing Li, Pengbin Gui, Borui Li, Chang Liu, Chen Tao, Qianqian Lin, and Guojia Fang. Room-temperature liquid diffused separation induced crystallization for high-quality perovskite single crystals. Nature Communications, 11(1), March 2020.

[22] Mingjian Yuan, Li Na Quan, Riccardo Comin, Grant Walters, Randy Sabatini, Oleksandr Voznyy, Sjoerd Hoogland, Yongbiao Zhao, Eric M. Beauregard, Pongsakorn Kanjanaboos, Zhenghong Lu, Dong Ha Kim, and Edward H. Sargent. Perovskite energy funnels for efficient light-emitting diodes. Nature Nanotechnology, 11(10):872–877, June 2016.

[23] Himchan Cho, Su-Hun Jeong, Min-Ho Park, Young-Hoon Kim, Christoph Wolf, Chang-Lyoul Lee, Jin Hyuck Heo, Aditya Sadhanala, NoSoung Myoung, Seunghyup Yoo, Sang Hyuk Im, Richard H. Friend, and Tae-Woo Lee. Overcoming the electroluminescence efficiency limitations of perovskite light-emitting diodes. Science, 350(6265):1222–1225, December 2015.

[24] T. Tiedje, E. Yablonovitch, G.D. Cody, and B.G. Brooks. Limiting efficiency of silicon solar cells. IEEE Transactions on Electron Devices, 31(5):711–716, 1984.

[25] Armin Richter, Martin Hermle, and Stefan W. Glunz. Reassessment of the limiting efficiency for crystalline silicon solar cells. IEEE Journal of Photovoltaics, 3(4):1184–1191, October 2013.

[26] Best Research-Cell Efficiency Chart — nrel.gov. https://www.nrel.gov/pv/cell-efficiency.html. [Accessed 26-Dec-2022].

[27] Giles E. Eperon, Tomas Leijtens, Kevin A. Bush, Rohit Prasanna, Thomas Green, Jacob Tse-Wei Wang, David P. McMeekin, George Volonakis, Rebecca L. Milot, Richard May, Axel Palmstrom, Daniel J. Slotcavage, Rebecca A. Belisle, Jay B. Patel, Elizabeth S. Parrott, Rebecca J. Sutton, Wen Ma, Farhad Moghadam, Bert Conings, Aslihan Babayigit, Hans-Gerd Boyen, Stacey Bent, Feliciano Giustino, Laura M. Herz, Michael B. Johnston, Michael D. McGehee, and Henry J. Snaith. Perovskite-perovskite tandem photovoltaics with optimized band gaps. Science, 354(6314):861–865, November 2016.

[28] Liuqi Zhang, Xiaolei Yang, Qi Jiang, Pengyang Wang, Zhigang Yin, Xingwang Zhang, Hairen Tan, Yang Yang, Mingyang Wei, Brandon R. Sutherland, Edward H. Sargent, and Jingbi You. Ultra-bright and highly efficient inorganic based perovskite light-emitting diodes. Nature Communications, 8(1), June 2017.

[29] Taame Abraha Berhe, Wei-Nien Su, Ching-Hsiang Chen, Chun-Jern Pan, Ju-Hsiang Cheng, Hung-Ming Chen, Meng-Che Tsai, Liang-Yih Chen, Amare Aregahegn Dubale, and Bing-Joe Hwang. Organometal halide perovskite solar cells: degradation and stability. Energy and Environmental Science, 9(2):323–356, 2016.

[30] Zhong He. Review of the shockley–ramo theorem and its application in semiconductor gamma-ray detectors. Nuclear Instruments and Methods in Physics Research Section A: Accelerators, Spectrometers, Detectors and Associated Equipment, 463(1):250–267, 2001.

[31] Ch. Honsberg a S. Bowden. Photon flux. Available from: https://www.pveducation.org/pvcdrom/properties-of-sunlight/photon-flux, 2020. [online].

[32] Sanford Wagner. Radiation detection: ¡i¿semiconductor detectors¡/i¿. g. bertolini and a. coche, eds. interscience (wiley), new york; north-holland, amsterdam, 1968. x + 518 pp., illus. $22.50. Science, 168(3930):462–462, 1970.

[33] L. Reggiani. Hot-Electron Transport in Semiconductors, volume 58 of Topics in Applied Physics. Springer Berlin Heidelberg, 1. edition, 1985. ISBN: 978-3662309353.

[34] Kazuhiko Suzuki, Takayuki Sawada, and Kazuaki Imai. Effect of dc bias field on the time-of-flight current waveforms of cdte and cdznte detectors. IEEE Transactions on Nuclear Science, 58(4):1958–1963, 2011.

[35] P.K. Kythe. Fundamental Solutions for Differential Operators and Applications. Birkhäuser, 1996.

[36] Jindřich Pipek. Charge transport in semiconducting radiation detectors. Master's thesis, 2018.

[37] A. Levi, M. M. Schieber, and Z. Burshtein. Carrier surface recombination in hgi2 photon detectors. Journal of Applied Physics, 54(5):2472–2476, May 1983.

[38] Karl Prof. Dr. Hecht. Zum mechanismus des lichtelektrischen primärstromes in isolierenden kristallen. Zeitschrift für Physik, 77:235–245, 1932.

[39] K. Suzuki and H. Shiraki. Evaluation of surface recombination velocity of cdte radiation detectors by time-of-flight measurements. In 2008 IEEE Nuclear Science Symposium Conference Record, pages 213–216, 2008.

[40] Carlo Jacoboni and Lino Reggiani. The monte carlo method for the solution of charge transport in semiconductors with applications to covalent materials. Rev. Mod. Phys., 55:645–705, Jul 1983.

[41] Marek Raja. Spektrální závislost generace náboje v polovodičových detektorech pomocí nanosekundových laserových pulsů. Master's thesis, 2020.

[42] Vikas Nandal and Pradeep R. Nair. Predictive modeling of ion migration induced degradation in perovskite solar cells. ACS Nano, 11(11):11505–11512, November 2017.

List of Figures

List of Abbreviations

$MAPbBr_3$ ..... Methylammonium lead tribromide perovskite

ToF ..... Time-of-flight method (spectroscopy)

μ ..... Drift mobility

μ_{eff} ..... Effective drift mobility

μ^e_{eff} ..... Effective electron drift mobility

μ^h_{eff} ..... Effective hole drift mobility

μ_{d_e} ..... Electron drift mobility

μ_{d_h} ..... Hole drift mobility

q ..... charge

m^* ..... Effective mass

$\langle\tau\rangle$ ..... Average scattering time

p ..... Hole concentration

t ..... Time

e ..... Elementary charge

$\mathbf{j}_h$ ..... Hole current density

G_h ..... Hole generation process

R_h ..... Hole recombination process

$\mathbf{E}$ ..... Electric field intensity

D_h ..... Hole diffusion coefficient

k_b ..... Boltzmann constant

T ..... Absolute temperature

n ..... Electron concentration

$\mathbf{j}_e$ ..... Electron current density

G_e ..... Electron generation process

R_e ..... Electron recombination process

D_e ..... Electron diffusion coefficient

$\mathbf{j}$ ..... Current density ($\mathbf{j} = \mathbf{j}_e + \mathbf{j}_h$)

U ..... Voltage, bias

$\mathbf{l}$ ..... Integration path

$\mathbf{v}_e$ ..... Electron drift velocity

$\mathbf{v}_h$ ..... Hole drift velocity

i ..... Instantaneous current

L ..... Detector length

I ..... Current

Q ..... Charge

SRT ..... Shockley-Ramo theorem

Φ ..... Photon flux

h ..... Planck's constant

λ ..... Wavelength

H ..... Area power density

δ ..... Dirac delta function

N_0 ..... Initial number of free holes in the valence band

χ ..... Boxcar function

τ_{tr} ..... Transit time

τ_T ..... Trapping time

τ_D ..... Detrapping time

N_T ..... Density of detention centers (traps)

E_T ..... Energy of traps in the band structure

N_C ..... Effective density of states in the valence band

σ_c ..... Effective capture cross-section

v_{vh} ..... Thermal velocity of free carriers

τ'_{tr} ..... Prolonged transit time due to the shallow trap

τ_{TS} ..... Trapping time of the shallow trap

τ_{DS} ..... Detrapping time of the shallow trap

τ_{TD} ..... Trapping time of the deep trap

τ_{DD} ..... Detrapping time of the deep trap

$\mathbf{D}$ ..... Electric displacement field

ε_r ..... Relative permittivity

ε_0 ..... Vacuum permittivity

Q_{in} ..... Charge in the Gaussian integration volume

ρ_0 ..... Space charge

E_ρ ..... Electric field created by the space charge

a ..... Slope of the linear electric field

E_{ext} ..... Electric field created by external source (bias el. field)

erf ..... Error function

tri ..... Triangle function

p_{bulk} ..... Probability of charge entering from surface layer to the bulk

s ..... Surface recombination velocity

Q_{00} ..... Photogenerated charge

Q_0 ..... Charge after surface recombination

CCE ..... Charge collection efficiency

$T+$ ..... Time width of the first bias pulse part

$T-$ ..... Time width of the second bias pulse part

$U+$ ..... Magnitude of the first bias pulse part

$U-$ ..... Magnitude of the second bias pulse part

LPD ..... Laser pulse delay

T_{depol} ..... Depolarization time

T ..... Period of bias pulse

$RX\#$ ..... Marking of samples